PASSIVE NOSETIP TECHNOLOGY (PANT) PROGRAM

VOLUME XXII. COUPLED EROSION/ABLATION OF REENTRY MATERIALS

ACUREX CORPORATION

PREPARED FOR
SPACE AND MISSILE SYSTEMS ORGANIZATION

JULY 1975

SAMSO-TR-74-86
Volume XXII

INTERIM REPORT
PASSIVE NOSETIP TECHNOLOGY
(PANT) PROGRAM

Volume XXII. Coupled Erosion/Ablation of Reentry Materials

C. J. Wolf
C. T. Nardo
T. J. Dahm

Aerotherm Division/Acurex Corporation

SAMSO-TR-74-86

July 1975

AEROTHERM REPORT 75-160

Air Force Space and Missile
Systems Organization
Los Angeles, California

Contract F04701-71-C-0027

C/N 7049.532

INTERIM REPORT
PASSIVE NOSETIP TECHNOLOGY
(PANT) PROGRAM

Volume XXII. Coupled Erosion/Ablation of Reentry Materials

C. J. Wolf
C. T. Nardo
T. J. Dahm

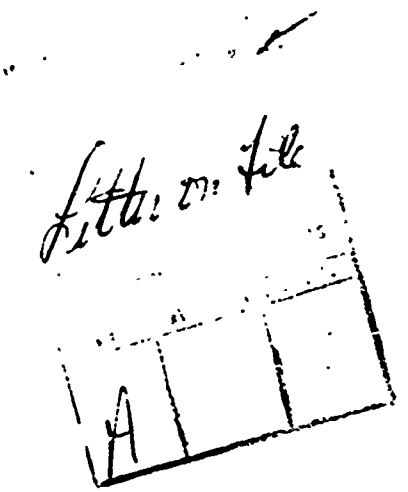

FOREWORD

This document is Volume XXII of the Interim Report series for the Passive Nosetip Technology (PANT) program. A summary of the documents in this series prepared to date is as follows:

Volume I – Program Overview (U)

Volume II – Environment and Material Response Procedures for Nosetip Design (U)

Volume III – Surface Roughness Data

Part I – Experimental Data

Part II – Roughness Augmented Heating Data Correlation and Analysis (U)

Part III – Boundary Layer Transition Data Correlation and Analysis (U)

Volume IV – Heat Transfer and Pressure Distributions on Ablated Shapes

Part I – Experimental Data

Part II – Data Correlation

Volume V – Definition of Shape Change Phenomenology from Low Temperature Ablator Experiments

Part I – Experimental Data, Series C (Preliminary Test Series)

Part II – Experimental Data, Series D (Final Test Series)

Part III – Shape Change Data Correlation and Analysis

Volume VI – Graphite Ablation Data Correlation and Analysis (U)

Volume VII – Computer User's Manual, Steady-State Analysis of Ablating Nosetips (SAANT) Program

Volume VIII – Computer User's Manual, Passive Graphite Ablating Nosetip (PAGAN) Program

Volume IX – Unsteady Flow on Ablated Nosetip Shapes – PANT Series G Test and Analysis Report

Volume X — Summary of Experimental and Analytical Results

Volume XI — Analysis and Review of the ABRES Combustion Test Facility for High Pressure Hyperthermal Reentry Nosetip Systems Tests

Volume XII — Nosetip Transition and Shape Change Tests in the AFFDL 50 MW RENT Arc — Data Report

Volume XIII — An Experimental Study to Evaluate Heat Transfer Rates to Scalloped Surfaces — Data Report

Volume XIV — An Experimental Study to Evaluate the Irregular Nosetip Shape Regime — Data Report

Volume XV — Roughness Induced Transition Experiments — Data Report

Volume XVI — Investigation of Erosion Mechanics on Reentry Materials (U)

Volume XVII — Computer User's Manual, Erosion Shape (EROS) Computer Program

Volume XVIII — Nosetip Analyses Using the EROS Computer Program

Volume XIX — Hydrometeor/Shock Layer Interaction Study

Volume XX — Investigation of Flow Phenomena Over Reentry Vehicle Nosetips

Volume XXI — Flight Implications of Low Temperature Ablator Shape Data

Volume XXII — Coupled Erosion/Ablation of Reentry Materials

Volume XXIII — Reentry Vehicle Nosetip Response Analyses

This report was prepared by Aerotherm Division/Acurex Corporation under Contract F04701-71-C-0027. Volumes I through IX covered PANT activities from April 1971 through April 1973. Volumes X through XV represent contract efforts from May 1973 to December 1974. Volumes XVI through XVIII describe the background, development, and check out of the PANT EROsion Shape (EROS) computer code. These volumes document efforts performed under supplementary agreements to the Minuteman Natural Hazards Assessment program (Contract F04701-74-C-0069) between April 1974 and March 1975. Volumes XIX through XXIII document additional analyses performed between December 1974 and June 1975.

This work was administered under the direction of the Space and Missile Systems Organization with Lieutenant A. T. Hopkins and Lieutenant E. G. Taylor as Project Officers with Mr. W. Portenier and Dr. R. L. Baker of the Aerospace Corporation serving as principal technical monitors. Mr. C. J. Wolf was principal Aerotherm investigator for the work described in this volume.

This technical report has been reviewed and is approved.

E G Taylor

E. G. Taylor, Lt. USAF
Project Officer
Aero and Materials Division
Directorate of Systems Engineering
Deputy for Reentry Systems

ABSTRACT

A study of coupled erosion/ablation effects in flight and ballistic range environments is conducted with the objectives of identifying and quantifying the sources, magnitudes and consequences of uncertainties associated with the data and phenomenology on which shape change calculations are based.

The interactions of the phenomena of temperature dependent single impact mass loss and erosion induced augmented heating as key elements within the morphology of coupled effects are investigated. It is found that for ATJ-S graphite, data scatter in single impact experiments is quantitative related to expected sample-to-sample variations of material strength and failure properties and that a correlation of mass loss data with these temperature dependent material properties suggests that the mass loss ratio increases with temperature above 6000°F.

It is shown, in situations important from both a design and a phenomenological point of view, that the effect of existing erosion augmented heating models is to bring about surface temperatures that significantly exceed the temperature range of the present single impact data base. The cumulative effect of the uncertainty associated with these factors, when combined with estimates of the uncertainties in other coupled effects, is shown to be comparable with the scatter observed in ballistic range data.

A test plan consisting of complimentary single impact and ballistic range experiments is presented in which the material samples, the impacting particle, the impact velocity and the thermal state of the material is closely matched. This test plan specifically addresses the problems of relating single impact data to circumstances where coupled erosion/ablation effects are important in that

1. Material property variations effecting the comparison between single impact and ballistic range tests are minimized.
2. The discrimination of obscuration and predamage effects in single vs. multiple impact situations is optimized within the constraint of current experimental procedure and apparatus.
3. A comparison and evaluation of erosion augmented heating models is facilitated.

TABLE OF CONTENTS

LIST OF ILLUSTRATIONS

LIST OF TABLES

LIST OF SYMBOLS

A	a constant in a mass loss expression
AH	augmented heating
B	a constant in a mass loss expression
BR	ballistic range
C	acoustic velocity = $\sqrt{E/\rho_t}$
C_c	acoustic velocity = $\sqrt{E_{AC}/\rho_t}$
C_o	dynamic sound speed
C_T	acoustic velocity = $\sqrt{E_{AT}/\rho_t}$
C_{HL}	laminar flow Stanton number
C_{HLR}	laminar-roughness augmented Stanton number
C_{HLS}	laminar-erosion augmented Stanton number
d_p	particle diameter
E	Young's modulus
f	frequency of particle impact
FKLR	laminar-roughness augmented heating factor
FKLS	laminar-erosion augmented heating factor
G	mass loss ratio = m_t/m_p
G_s	single impact mass loss ratio
k	the total number of variables in a mass loss expression
k_c	crater roughness height
k_i	intrinsic roughness
ℓ_m	mean distance between particles in a cloud

LIST OF SYMBOLS (Continued)

L	length of erosive field in ballistic range
m_p	particle mass
m_t	target mass loss
$\dot{m}_E$	erosion mass loss rate
n_i	exponent on a variable in a mass loss expression
N	average number density
p	crater penetration depth
S	ultimate tensile strength
$\dot{S}_A$	ablation component of surface recession rate
$\dot{S}_E$	erosion component of surface recession rate
$\dot{S}_T$	total surface recession rate
SI	single impact
SURFEB	surface energy balance
T	temperature
V	velocity
$\overline{V}$	volume swept out by ballistic range model
w	particulate field concentration
X_i	a general variable in a mass loss expression
Y	dynamic yield strength in shear
Z	a variable with the dimensions of stress
ε	strain to failure
θ	impact angle

ρ_p	particle mass density
$\sigma_{( )}$	standard deviation of the variable ( )
ν	Poisson's ratio
$\mu_{( )}$	mean of the variable ( )

Subscripts

AC	across grain – compressive
AT	across grain – tensile
e	edge of boundary layer
i	a variable identification index
TF	threshold for tensile failure
∞	free stream

Superscripts

$( )^\circ$	observed value of ( )

SECTION 1

INTRODUCTION

During the past several years, significant efforts have been directed towards the erosion characterization of candidate RV nosetip materials. These efforts have met with partial success in that the functional dependence of hypervelocity impact mass loss on certain of the impact variables (such as particle velocity) have been well established. However, the scatter in erosion mass loss data, in both single impact tests and ballistic range experiments, still indicates a serious deficiency in the erosion mass loss laws. Data scatter of the order ± 50 percent is common with many data indicating scatter in both directions by factors greater than 2. This level of uncertainty in predicting erosion mass loss can result in a serious error in predicting overall RV system performance. Advanced mission concepts and systems planning will require RV systems with improved performance and accuracy over those which currently exist. In addition, the natural hazards penetration capability of the RV will also necessarily have to be improved. To achieve this greater RV system performance in erosive environments, current coupled erosion/ablation modeling techniques need to be improved. Improved modeling, however, requires an understanding of the current erosion data and its tendency to produce large data scatter. As a result, a study program was undertaken with the objectives of critically assessing the existing erosion data base and identifying the sources and contribution of various material parameters (both target and projectile) to the overall erosion data scatter that is currently observed.

The approach utilized in this study was one in which the various inputs and data that enter into a coupled erosion/ablation prediction were identified. A systematic approach was then formulated in which the data were discriminated and categorized according to criteria that would improve understanding of the scatter.

In Section 2, a description of the various elements that enter into a coupled erosion/ablation prediction is presented. It is shown that a key element that contributes significantly to an accurate calculation includes target material strength parameters. In Section 3, a detailed discussion of the scatter in single impact data on ATJ-S polycrystalline graphite is

presented. It is observed that material strength property uncertainties can, in fact, explain most of the data scatter observed in single impact data. In Section 4, a description of ballistic range data and its association with single impact data is presented. A discussion is also given in which the implications of the current erosion data base on flight data predictions is examined.

Section 5 details the recommendations and conclusions that result from the study and, in addition, recommends a single impact/ballistic range test plan that addresses the uncertainties and concerns that were identified during the course of this investigation. The supporting technology for this recommended test program is given in the Appendix.

SECTION 2

MORPHOLOGY OF COUPLED EROSION/ABLATION SHAPE CHANGE

The flow chart shown in Figure 1 indicates the principle components and their interrelationships for the calculation of coupled erosion/ablation shape change. It is apparent from Figure 1, that the basic inputs to a coupled shape change calculation are the weather and the trajectory. The trajectory is the determining factor for the thermal environment to which the nosetip is exposed and, along with the instantaneous shape, determines the shock shape and standoff distance which is of the first order importance in the interaction between the constituents of the weather (rain, ice or snow) and the shock layer. The definition of the weather should, in principle, include the mass content, the size distribution and the particle type for the cloud encountered. It is these quantities plus the nature of the shock layer that are essential for the application of hydrometeor deceleration, breakup and demise models. The output of this element, then, is the size, mass and velocity (vector) distributions of the particles that impact on the nosetip.

The element that is basic to erosion in a coupled calculation is the mass loss that results from the impact of a single particle at a given location on the nosetip. For the impact of a particle with a specified mass (and possibly density) and velocity, the primary variables of the nosetip material that determine mass loss are its "strength" and density. Strength, as used here, includes the state of the target material as a result of predamage, thermal stress, aerodynamic stress, temperature dependent material properties, etc. The density may also be a function of the heating rate, as is the case for a charring ablator. The thermal state of the nosetip is, in turn, determined by the result of the surface energy balance. Assuming, for the purpose of illustration, that the complete state of the nosetip material is known so that the mass loss ratio, G_s, is also known, then the combination of G_s and the rate at which particles impact (from the shock layer interaction model) determines the rate of mechanical mass loss. If the target material undergoes a change in its impact response due to previous impact(s), then there is coupling (or feedback) to the element that represents the state of the target material. This interaction is through the element identified as "obscuration" in

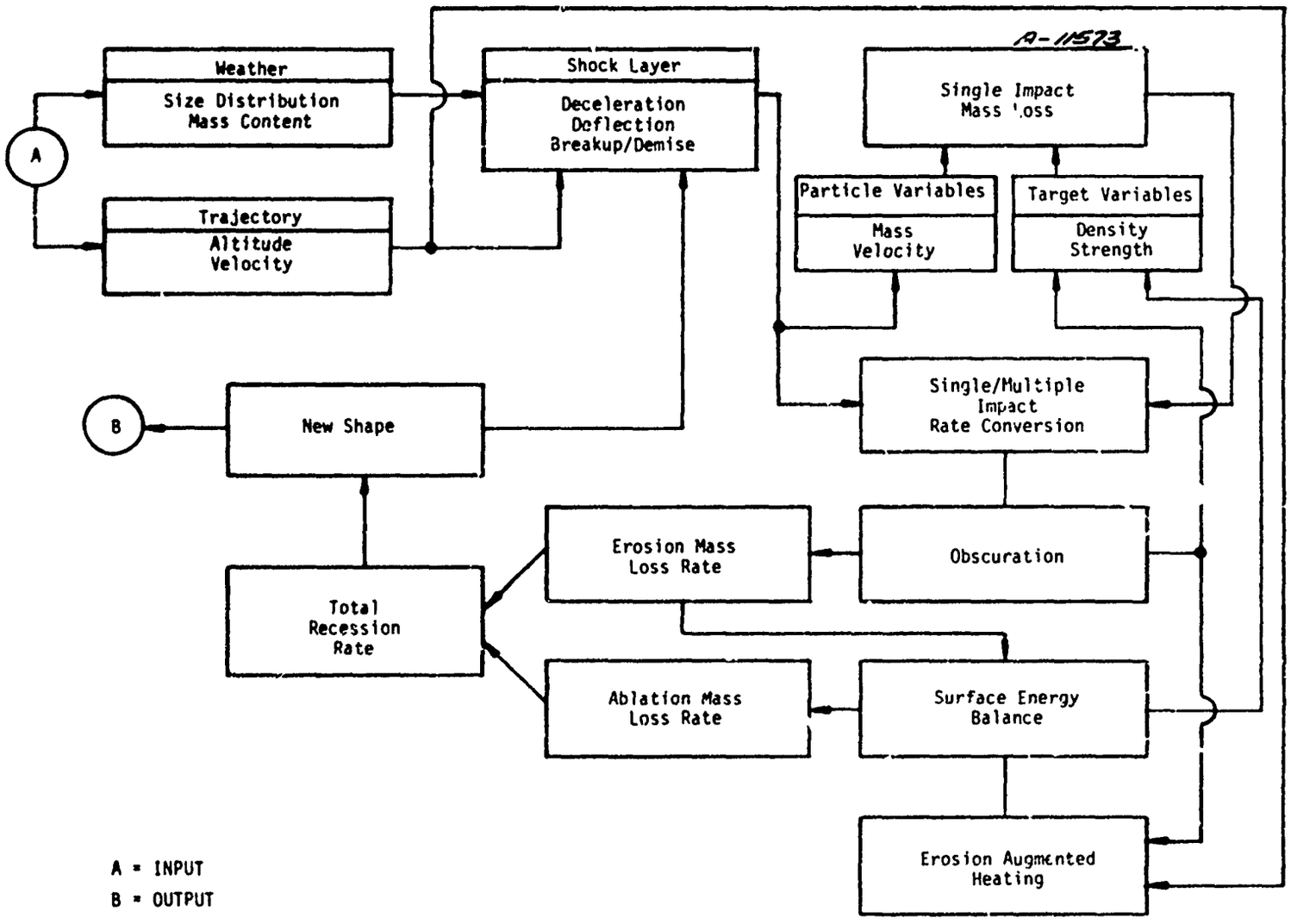

Figure 1. Morphology of coupled erosion/ablation shape change.

Figure 1, which accounts for the probability that a given location on the target will have been previously impacted.

The net surface recession rate is composed of an erosion component and an ablation component, but as shown in Figure 1, they are not independent. The erosion mass loss rate is directly involved in the surface energy balance as well as being input to the heating augmentation models. The erosion and ablation components of shape change are, therefore, seen to be coupled in a variety of ways through different phenomena.

A major objective of the present work is to examine different aspects of this coupled process in order to identify and quantify specific sources of uncertainties and to trace through the cumulative effect of these uncertainties. In this context, it is important to recognize that for an experiment in which coupled effects are present, such as a ballistic range shot, there is no explicit method of separating the erosion and ablation components from the measured total surface recession. Therefore, an expedient and logical approach is to first examine the experiments for which coupled effects are not present. In addition, this discussion is restricted to the erosion response of ATJ-S graphite only for purposes of being explicit.

SECTION 3

SINGLE IMPACTS INTO ATJ-S GRAPHITE

Since the result of a single impact event is central to an erosion calculation, it is relevant to examine this situation at first in a context isolated from coupled effects. What is sought is an understanding and a quantification of the sources of data scatter in single impact experiments. To this end, Section 3.1 gives a compilation of single impact data for ATJ-S and some estimates of experimental uncertainties. Section 3.2 discusses material property dependent mass loss expressions and Section 3.3 identifies sample to sample variation of material properties as a major contributor to single impact data scatter.

3.1 SINGLE IMPACT DATA

A survey of the literature and personal communication with some of the authors of recent reports has identified data from about 50 single impact experiments on ATJ-S graphite. Some of the data are as yet unpublished, however, they are reasonably accessible. The data were obtained mostly from the Science Applications Incorporated (SAI) facility, previously owned by KMSI, and the Effects Technology Incorporated (ETI) facility. These data are reported by Sullivan (Reference 1) and Rubin, et al. (Reference 2). Other data taken at these facilities were obtained from Rubin (Reference 3). The remaining data are from AVCO and are reported by Reinecke, et al. (Reference 4). A survey describing these facilities is given by Dahm, et al. (Reference 5) and further details on the ETI facility are given by Graham, et al. (Reference 6).

In addition to the data, information on the experimental errors associated with the measurement of various parameters has been collected. The sources for some of this information are Graham, et al. (Reference 6), Graham (Reference 7), and Rubin (Reference 3).

The data and the estimated errors are shown in Table 1, which also identifies the source of the information and contains some comments on experimental methods and circumstances. It is seen from Table 1 that the experiments cover a temperature range from T = 530°R to about 6000°R, velocities up to V = 15 kfps, particle diameters from d_p = 300 μm to 2290 μm and particle mass densities of ρ_p = 0.92 gm/cc and = 2.5 gm/cc. Other quantities listed in Table 1 are:

TABLE 1. SINGLE IMPACT DATA AND UNCERTAINTIES FOR ATJ-S

Source	Facility	Particle Material	d_p[1] (μm)	Δd_p (%)	ρ_p (gm/cm)	$\Delta\rho_p$ (gm/cc)	M_p (mg)	ΔM_p (μg)	ΔM_t (μg)	Measurement Method	G/G_o[3]	V_p (fps)	V_p (°)	(deg)	T (°R)
Ref. 1	KMSI	Rain[2]	1000				0.9			Weight	0.88	10,000		90	[illegible]
	KMSI		1000				0.8				2.22	9,850			4100
	KMSI		1000				0.8				2.59	10,050			415[illegible]
	KMSI		1500				2.8				0.88	9,850			535
	KMSI		1500								1.10	9,750			535
	KMSI		1500								0.91	9,750			535
	KMSI		1500								5.91	10,800			2510
	KMSI		1500								1.84	10,200			2340
	KMSI		1500								1.51	10,150			4170
Ref. 2	SAI	Glass	520		2.42	±0.25	0.172	±1.0	±100		0.66	8,480	+5/-3		900
	SAI		520								0.58	8,350			
	SAI		520								0.50	8,420			
	SAI		520								0.74	8,370			
	SAI		520								0.80	8,900			
	SAI		520								1.38	12,000			
	SAI		520								1.26	12,200			
	SAI		520								1.04	10,400*			
	SAI		520								1.12	10,200*			
	SAI		1000				1.420				1.41	12,600			
	SAI		1000				1.420				1.37	12,200			
	SAI		840				0.850				0.87	10,000			
	SAI		840								0.76	9,900			
	SAI		840								0.84	10,000			
	SAI		840								0.89	9,500			
	SAI		840								0.78	9,900			
	SAI		840								1.06	10,000			
	SAI		840								0.97	9,280			
	ETI		520	±2	2.54	±0.5%	-0.168		±5%		0.56	9,300	±5		
	ETI		520								0.60	8,800			
	ETI		520								1.56	12,100			
	ETI		520								1.33	11,000			
	ETI		520								0.96	11,600			
	ETI		520								1.37	12,300			
	ETI		520								1.22	11,800			
	ETI		520								1.21	12,900			
	ETI		520								1.29	13,000			
	ETI		1000				-1.460				0.54	8,500			
	ETI		1000								0.53	8,200			
	ETI		1000								1.29	12,300			
	ETI		1000								1.30	11,700			
	ETI		300				-0.038				1.03	11,300			
	ETI		300								.02	11,700			
Ref. 3	AVCO STP	Ice	2290		0.92			±0.1	±100		0.28	4,200			
	AVCO STP		2290								0.33	4,500			
	AVCO STP		2290								0.67	8,800		45	
	AVCO STP		2290								1.54	11,100		90	
	AVCO STP		2290								0.22	11,500		20	
	AVCO STP		2290								0.20	4,300		45	
	AVCO RADEF	Polyethylene	1000				-0.5				0.36	5,000		90	
	AVCO RADEF		1000								0.43	5,000			
	AVCO RADEF		1000								0.22	4,900			
	AVCO RADEF		1000								0.50	5,000			
	AVCO RADEF		1000								2.19	10,500			
	AVCO RADEF		1000								1.91	10,200			
Ref. 4	SAI	Glass	520		2.42	±0.25	0.172	±1		Beeswax Fill	1.32	12,100	+5/-3		4660
	SAI		520								1.10	12,200			5060
	SAI		520								0.93	12,200			960
	SAI		520								1.05	11,300			6060
	SAI		520									7,800			4760
	SAI		520									8,100			4660
	SAI		520									8,300			5960
	SAI		520									3,100			5960

Notes: 1. Values shown are nominal diameters of nearly spherical particles.
2. Encapsulated in plastic.
3. $G_o = AV^{1.72}$, V = 10 kfps (Table 4).

θ = impact angle

m_p = particle mass

G = mass loss ratio = m_t/m_p (where m_t = mass lost from target)

and the estimated experimental erros for these quantities which are indicated by the prefixed Δ. The particle material is also shown as well as the method that was used to measure the mass loss, i.e., by weighing the target before and after impact or by measuring the volume of the crater.

Summarizing the estimated experimental errors shown in Table 1, it is judged reasonable to assign the following standard deviations (σ) as fractions of the means (μ) of the variables.

$\sigma_{m_p} = 0.001\ \mu_{m_p}$

$\sigma_{\rho_p} = 0.10\ \mu_{\rho_p}$

$\sigma_{d_p} = 0.10\ \mu_{d_p}$

$\sigma_v = 0.05\ \mu_v$

$\sigma_{m_t} = 0.04\ \mu_{m_t}$ by weighing

$\sigma_{m_t} = 0.08\ \mu_{m_t}$ by volume

In most cases, these estimates are based on the resolution limits of the instrumentation quoted by Graham, et al. (Reference 6) and Graham (Reference 7), and as such do not include contributions due to other random errors (possibly procedural). It has been assumed that the experiments were carefully conducted and that these contributions are minimal. Some exceptions to this method of assigning σ must be noted, however. With regard to particle properties, they are, of course, measured before launch, and for the diameter and mass density, only nominal values can be assigned. The reason is that glass beads, for example, are slightly nonspherical and contain small voids. Therefore, the standard deviations for ρ_p and d_p are assigned on the basis of what is judged to be the upper limit for all of the data in Table 1. When the mass lost by the target can be measured by weighing (room temperature test), the resolution of the scale is ± 1 µgm, resulting in the assigned value for σ_{m_t}. However, at high temperatures, the target suffers ablation mass loss if heated by an arc jet and collects debris from insulation material if inductively heated. Consequently, it is standard practice to measure the volume of a crater by filling it with a suitable material (e.g., beeswax or mercury) of known density. This volumetric method is less accurate than the weighing method because of the possibility that the crater is not completely filled and because the bottom of the crater may contain

crushed target material with density larger than the density of the bulk material. Thus, there is a discrepancy between the results of mass and volumetric methods even when used on the same room temperature test sample. In view of the considerations, σ_{m_t} has been somewhat arbitrarily assigned a value of 0.08 μ_{m_t}, which is believed to be reasonable and is consistent with the judgement of Rubin (Reference 8).

On Figure 2, the single impact data of Table 1 are compared to the correlation

$$G = Av^{1.72}$$

in which the exponent on velocity was taken from a regression analysis (of part of the data) by Benjamin (Reference 9) and the coefficient was chosen so as to give an approximately least squares fit to the data. Also shown on Figure 2 are lines indicating ± 40 percent of the correlation which are seen to bracket nearly all the data. The major exceptions are a group of early data obtained at the KMSI facility and reported by Sullivan (Reference 1) and Benjamin (Reference 9). This set of data have been questioned (see Benjamin, Reference 9, for example) and justification for the exclusion of these data can be given. However, these considerations are unnecessary for the present purposes, because it is sufficient here to have only a rough estimate of the overall scatter in the data.

The important point is that the overall scatter is significantly larger than can be explained by experimental uncertainties. This can be seen by noting that with

$$\sigma_G^0/\mu_G^0 = 0.4$$

where $(\ )^0$ means "observed" in the data, only a small part of the scatter is due to the experimental measurement of mass loss. Specifically,

$$\left(\frac{\sigma_G^0}{\mu_G^0}\right)^2 = \left(\frac{\sigma_G}{\mu_G}\right)^2 + \left(\frac{\sigma_{m_t}}{\mu_{m_t}}\right)^2 + \left(\frac{\sigma_{m_p}}{\mu_{m_p}}\right)^2$$

where σ_G is the standard deviation of the component of the scatter due to variations in the dependent variable(s), which, in turn, is determined by the mass loss expression and the standard deviations of those variables. When G is of the form

$$G = \prod_{i=1}^{k} X_i^{n_i} \qquad (1)$$

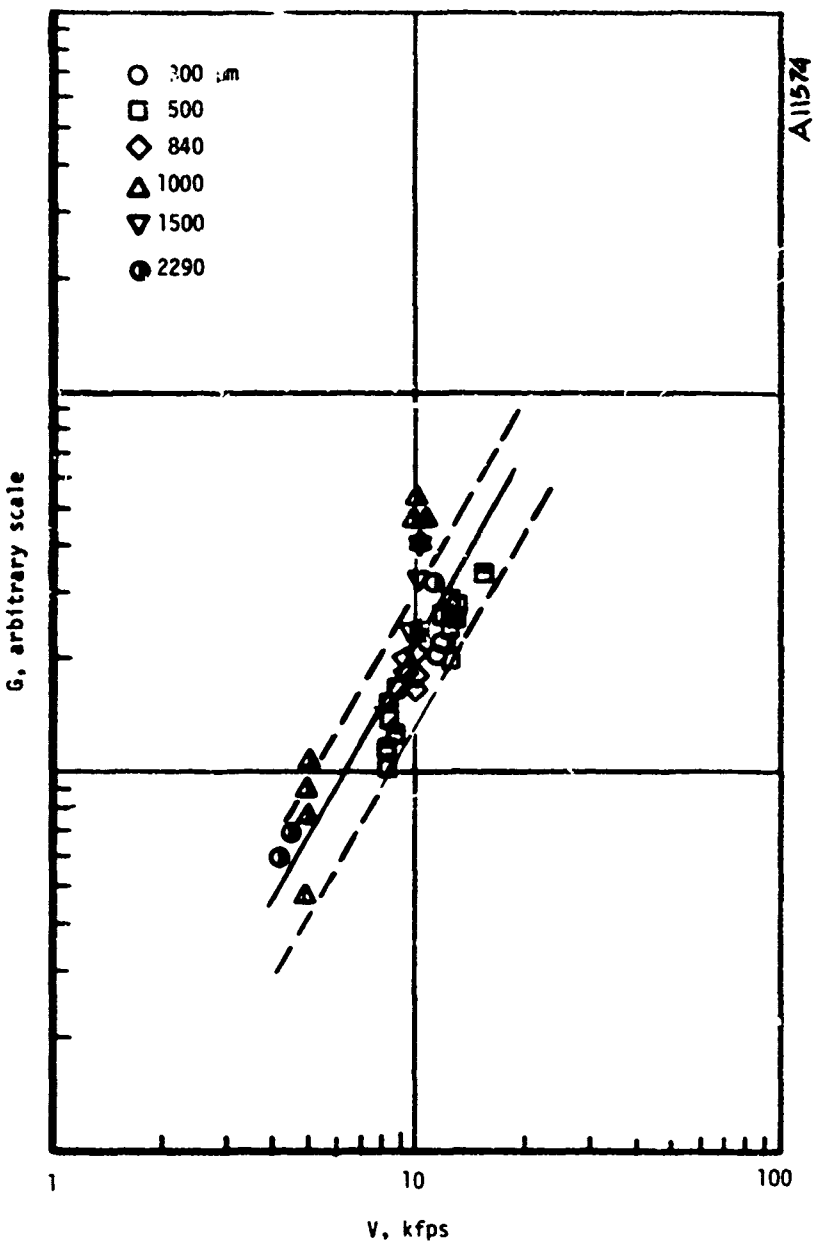

Figure 2. Comparison of single impact data with correlation and estimated standard deviation.

then

$$\left(\frac{\sigma_G}{\mu_G}\right)^2 = \sum_{i=1}^{k} \left(n_i \frac{\sigma_{x_i}}{\mu_{x_i}}\right)^2 \qquad (2)$$

where the X_i are the independent variables. Thus, with

$$G = KV^{1.72}$$

(i.e., with velocity as the only independent variable) one finds that

$$\sqrt{\left(\frac{\sigma_G}{\mu_G}\right)^2 + \left(\frac{\sigma_{m_t}}{\mu_{m_t}}\right)^2 + \left(\frac{\sigma_{m_p}}{\mu_{m_p}}\right)^2} = 0.1175 \frac{\sigma_G^0}{\mu_G^0}$$

The conclusion is, then, that there are missing variables in the mass loss expression and that variations of these factors contribute significantly to the overall data scatter.

In order to identify these variables, the next section examines the problem of generalizing mass loss expressions to include dependence on material properties. In Section 3.3, it is shown that reasonable forms of mass loss expressions and existing data on material property variability lead to estimates of data scatter that are in better agreement with observations.

3.2 MATERIAL PROPERTY DEPENDENT EROSION

It is intuitatively obvious and easy to show by dimensional analysis that the result of a hypervelocity impact depends on the material properties of the target and the particle. It is very difficult, however, to identify the most important properties and the appropriate functional forms. The reasons for the difficulties are that the stress levels and strain rates imposed on materials by a hypervelocity impact are orders of magnitude larger than what is achievable by standard material testing apparatus. As a result, the constitutive equations appropriate to the circumstances are simply not well known.

It follows that theoretical understanding of the phenomenon is incomplete. However, it is nevertheless useful to examine the theories in order to obtain what available guidance there is for the inclusion of material properties in mass loss expressions.

3.2.1 Theoretical Guidelines

The theories may be broadly classified as hydrodynamic, quasi-dynamic-elastic and hydrodynamic-plastic-elastic. Theories of the hydrodynamic type (see Rae, in Reference 10, for a survey) are based on the equations of motion of an inviscid compressible fluid. The hydrodynamic theories are, therefore, limited in applicability to the earliest stages of impact and involve material properties only as they appear in the equation of state. These theories have led to some very general results such as late stage equivalence. However, mass loss is not predictable by hydrodynamic theories, which are, therefore, not useful in the present context.

The quasi-dynamic-elastic theory of Greszczuk (Reference 11) treats the stress field in the target by the methods of linear elasticity (following Timoshenko, et al. (Reference 12)) assuming that at each instant the load is due to the time dependent surface pressure distribution under the impactor. With this theory, it is possible to calculate a threshold impact velocity at which stress equals an assigned value of ultimate strength in compression, tension or shear. A typical result for a threshold velocity (the velocity required to cause a tensile failure) is

$$V_{TF} = 24.33\, S^{5/2}\, \rho_p^{-1/2}\, E^{-2}\, (1 - 2\nu)^{-5/2}\, (1 - 2\nu^2)^2$$

where S = ultimate tensile strength

E = Young's modulus

ν = Poisson's ratio

ρ_p = mass density of impacting particle

It appears that this theory is of some use as a guide for selection of impact resistant materials. Yet it is clear that it is a much simplified model of an impact event, since for example, no details about the crater or mass loss are obtainable. The underlying question is also not directly addressed by this work, which is; what is the proper stress-strain relationship at very high pressure and strain rate?

The hydrodynamic-plastic-elastic theories are, at present, the only analyses that deal with the full complexity of an impact. The method is to solve numerically the equations of motion for the particle and the target. Such numerical models are necessarily more opaque than analytic ones, but they seem essential to the solution of the problem because every known detail can (in principle) be incorporated. In fact, it appears that current codes for the

numerical solution of impact problems are nearly complete as far as the basic methodology is concerned. The remaining problem areas are basic to the phenomena and concern the constitutive and state equations that are input to the codes. Since these questions are the subject of continuing research, complete and definitive results are not yet available.

Of the existing numerical results, a series of calculations with an Eulerian code at Systems, Science and Software, Incorporated (S^3) for impact into a ductile metal (aluminum) were correlated by Walsh and Sedgwick (Reference 13) as

$$\frac{P}{d_p} = 0.482 \left(\frac{\rho_p}{\rho_t}\right)^{0.537} \left(\frac{V}{C_o}\right)^{0.576} \left(\frac{Y}{\rho_t C_o^2}\right)^{-0.235}$$

in which P = crater penetration depth

C_o = dynamic sound speed

Y = dynamic yield strength in shear

This equation was obtained from a matrix of calculations in which the parameters were systematically varied and was also shown to give good agreement with experiment. Although it is not directly applicable to A-3-S, it is useful in that it suggests a mass loss expression of the form

$$G \propto \frac{\rho_t P^3}{\rho_p d_p^3} \propto \left(\frac{\rho_p}{\rho_t}\right)^{0.611} \left(\frac{V}{C_o}\right)^{1.728} \left(\frac{Y}{\rho_t C_o^2}\right)^{-0.705}$$

According to Gurtman (Reference 14) recent calculations for graphite have been carried out but are not yet in final form, hence the above expression may at some later date be given a more definitive form.

Another series of numerical calculations with a different code has been reported by Kreyenhagen, et al. (Reference 15). The code is of the "particle in the cell" type for the initial hydrodynamic phase of the impact. At later times in the solution, when strength properties begin to affect the material response, a transition to a Lagrangian computational method is made.

The constitutive equations for the Lagrangian phase of the deformation were elastic-plastic with a von Mises yield criterion. The material model is representative of graphite at 4000°F, in that brittle failure in tension and cracking occur when the stress exceeds an assigned value.

Many detailed results, showing crater shape and residual cracks, for example, are given by Kreyenhagen, et al. (Reference 15). For the present purposes, however, the main result is that among the available solutions enough separate cases have been calculated so that a first order correlation can be constructed. The basic elements of this correlation are dimensional analysis, simple analytical forms and solutions at two impact velocities, for two particles (water and silica) and for two values of the "yield strength" in tension. These considerations give

$$G \propto \left(\frac{\rho_p}{\rho_t}\right)^{-0.436} \left(\frac{\rho_p V^2}{S}\right)^{0.722} \left(\frac{Z}{S}\right)^{1.218}$$

where S = ultimate tensile strength

Z = a quantity with the dimensions of stress (necessary for dimensional reasons but not determined by available solutions)

A later series of calculations have been undertaken at California Research and Technology (CRT), in which, according to Rosenblatt (Reference 16), changes to the constitutive equations have been instituted. The results of calculations with the modified material model have been compared with the data of Rubin, et al. (Reference 2), however, parametric studies are not yet available.

In spite of the incomplete nature of these numerical calculations, study of the results and modeling used in the construction of the theories yields much insight and qualitative understanding of an impact event. In the following, the feasibility of incorporating some of these ideas in mass loss expression for ATJ-S graphite is examined with the aid of the additional information provided by the recent data of Rubin, et al. (Reference 2) on the temperature dependence of mass loss.

3.2.2 Incorporation of Experimental Results

While data are admittedly sparse (consisting of four points at two velocities and two temperatures), they are most likely the highest quality data to date. As shown in Figure 3, in the range from 4500°F to 5500°F, the mass loss ratio for ATJ-S decreases with increasing temperature. This behavior is qualitatively explained by Rubin, et al. (Reference 2) with the observation that the material becomes relatively more ductile with increasing temperature. The mechanical properties of a material most closely associated with its ductility are tensile modulus and strain to failure. The trends of tensile ductility and strain to failure with

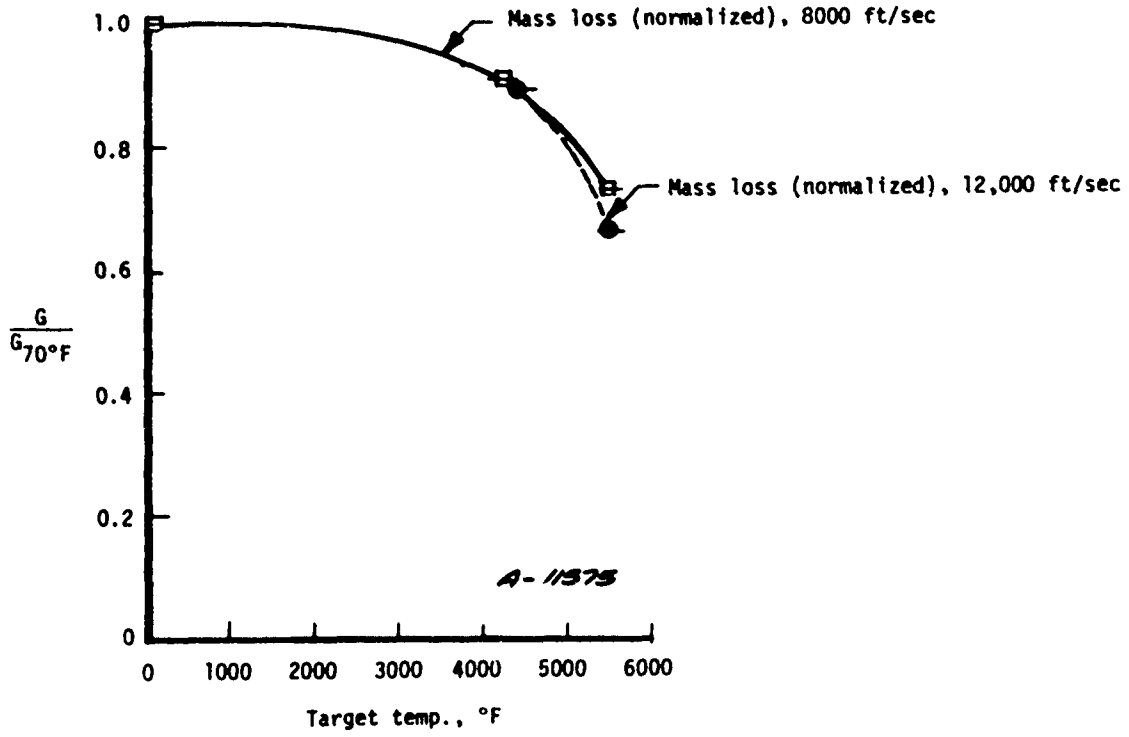

Figure 3. Experimental mass loss dependence on temperature of ATJ-S, from Rubin and McClelland (Reference 2).

temperature for ATJ-S are consistent with this observation and appear to be the basis for the suggestion by Rubin, et al. (Reference 2) that they may be correlating parameters. A more comprehensive compilation of the mechanical properties of ATJ-S is given by Starrett and Pears (Reference 17), which shows in greater detail the behavior of ATJ-S at elevated temperatures.

What is sought here is a dimensionally consistent combination of mechanical properties as functions of temperature that, when combined with other appropriate variables, correlate the observed mass loss vs. temperature data. Since the impact velocity is the primary variable in a mass loss expression, dimensional considerations dictate a combination like

$$\frac{\rho V^2}{S} \quad \text{or} \quad \frac{V}{C}$$

where S has the dimensions of stress and C has the dimensions of velocity. Because of the success of the S^3 correlation cited earlier, the incompleteness of other studies and the apparent ductility of ATJ-S at high temperature, the most justifiable choice appears to be V/C. From an empirical point of view, there is little to distinguish between the two because both quantities, either taken directly from Starrett and Pears (Reference 17) such as

$$S(T) = \text{ultimate tensile strength}$$

or calculated, for example, as

$$C(T) = \sqrt{E(T)/\rho_t}$$

where $E(T)$ = Young's modulus

have essentially the same temperature dependence, although somewhat out of phase. These two dimensionless groups as functions of temperature are compared in Figure 4, for which the exponents on the dimensionless groups have been taken following the correlations discussed above. It is seen that the normalization with C reaches a minimum at about 3200°F whereas with S, the minimum is at about 4500°F. The (V/C) group is also somewhat smoother in the temperature range of interest (as measured by changes in slope).

With either of these combinations and the data of Rubin, et al. (Reference 2), it is possible to deduce the temperature dependence of whatever other combination of properties appear in the mass loss expression. These manipulations result in ratios:

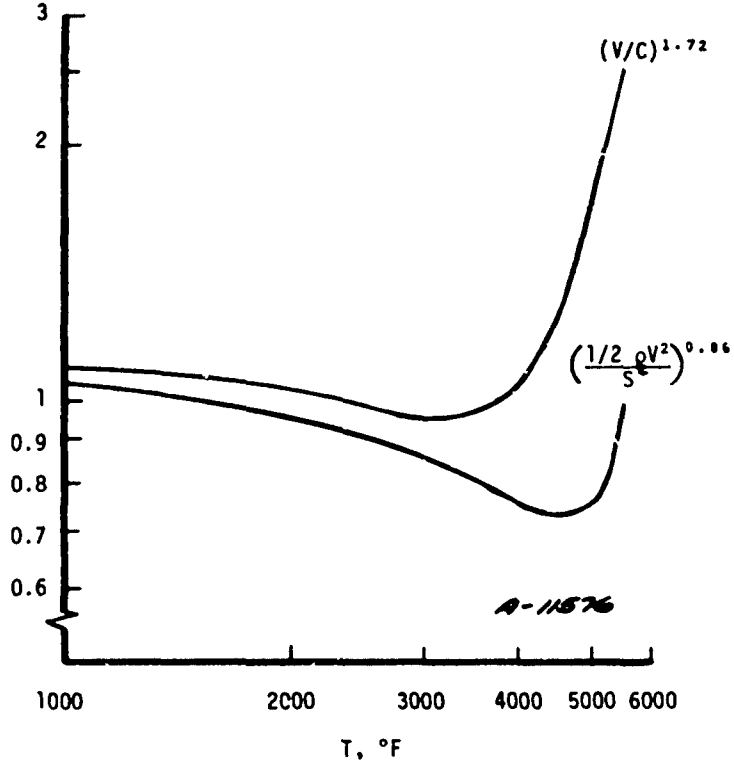

Figure 4. Comparison of temperature dependent velocity normalizations; relative to room temperature values.

$$\frac{G_{measured}}{\left(\frac{V}{C}\right)^{1.72}} \quad \text{or} \quad \frac{G_{measured}}{\left(\frac{\rho_t V^2}{2S}\right)^{0.86}}$$

versus temperature that decrease with increasing temperature (with similar slopes). Therefore, a complete mass loss expression must include a factor which is a function of material properties that has the same temperature dependence as these ratios.

The choice among the remaining easily accessible material properties is rather more difficult. The material strengths that are used in the numerical calculations are not the same as the ultimate strengths (for example) that are determined by standard material testing. Hence, the most that can be achieved is to find a combination of the better known material properties that give a reasonable correlation of the dynamic properties. It should also be pointed out, that the main objective of this aspect of the present study is to facilitate the estimation of the contribution of property variations to observed data scatter. For this purpose, statistical information is necessary, which is available for ordinary material properties, but not for such difficult to measure quantities as dynamic shear strength.

A number of combinations of tensile, compressive and shear modulii and associated ultimate strengths vs. temperature from the data of Starrett and Pears (Reference 17) and Shannon (Reference 18) were tested for suitability in the correlation. Both across grain and with grain properties of ATJ-S (which is slightly nonisotropic) were tried. Since for the data of Rubin, et al. (Reference 2), the impact velocity was parallel to the "across grain" direction, it seems reasonable to associate material failure modes during impact with this direction. Furthermore, the test for correlation did not indicate a clear choice, hence, the properties measured across grain were decided upon.

When an additional parameter with the dimensions of stress is included in the correlation, it must be combined with either ρC^2 or a third parameter of the same dimensions. Some of these combinations can be eliminated from consideration because the resulting trend with temperature is inconsistent with the requirements of the correlation. Among the other possibilities, the choice is a matter of judgement. For the present, it is suggested that tensile strain to failure is the most probable candidate. There are a number of reasons for this choice, among the most important being that strain to failure vs. temperature has a trend easily associated with the mass loss vs. temperature data, as pointed out by Rubin, et al. (Reference 2). Additional support for this choice comes from the observation that material response to an impact should be correlated with some measure of the plastic flow and failure

properties of the material. This is an intuitatively appealing conjecture and is supported by certain aspects of the modeling and the results of the numerical studies. Whether or not further basic research on the hypervelocity impact response of graphite will support these conjectures in detail is unknown, but it is very plausible that mass loss depends at least on an elastic and a plastic/failure property of the material. For the present, it is necessary to rely on the foregoing intuitive and qualitative arguments, and the fact that elastic modulii and strain to failure are reasonably well known from experiments.

Two summary reports on ATJ-S material property data are the work of Starrett and Pears (Reference 17) and Channon (Reference 18). Starrett and Pears concentrate on the data taken at Southern Research Institute (SoRI) over the last few years. Channon (Reference 18) is an earlier work (1968) and uses a number of different sources. There are some differences in detail that result from the application of the correlation ideas given in the previous paragraphs to these two data sets.

With the distributions of elastic modulus and strain to failure vs. temperature given by Channon (Reference 18), a fit to the mass loss ratio data of Rubin, et al. (Reference 2) gives

$$G \propto \left(\frac{V}{C_T}\right)^{1.72} \varepsilon^{-1.69} \tag{3}$$

over the temperature range 4500°F $\leq$ T $\leq$ 5500°F and where

$$C_T = \sqrt{E_{AT}/\rho_t}$$

with

$$E_{AT}(T) = \text{tensile modulus across grain}$$

and

$$\varepsilon(T) = \text{strain to failure across grain}$$

A fit to the same data using the properties given by Starrett and Pears (Reference 17) gives

$$G \propto \left(\frac{V}{C_T}\right)^{1.72} \varepsilon^{-0.85} \tag{4}$$

or

$$G \propto \left(\frac{V}{C_C}\right)^{1.72} \varepsilon^{-1.08} \tag{5}$$

where

$$C_C = \sqrt{E_{AC}/\rho_t}$$

and

$$E_{AC}(T) = \text{compressive modulus across grain}$$

The main difference between these two sets of property data is in the high temperature range. The SoRI data on E_{AT} or E_{AC} extrapolates to zero (according to Starrett and Pears, Reference 17) at about 7000°F, whereas for the Aerospace data, E_{AT} extrapolates to zero at about 6000°F. For both sets of data, ε is available over a more limited temperature range than are the elastic properties. Therefore, in all calculations given here, ε has been linearly extrapolated from the last two data points. Also, the SoRI data on elastic modulii used here are those designated by Starrett and Pears (Reference 17) as "most probable" whereas the SoRI data on strain to failure are the reported means from a number of samples.

Thus, a combination of results from theoretical predictions of hypervelocity impact leads to a functional form for the mass loss ratio of graphite that includes material properties in dimensionless groups and some insights into the proper choice of variables. Additional intuitative arguments have been given to explain the choices of tensile elastic modulus and strain to failure. By comparison of the behavior of material properties vs. temperature with experimental single impact mass loss vs. temperature, further support for the choice of variables was found, and simple, first order mass loss correlations were developed. These correlations (which differ very slightly in the exponnets because of differences in reported values of material properties for ATJ-S) give a reasonable fit to current mass loss data in the temperature range 4500°F to 5500°F.

Since, as will be shown, hypervelocity impact events can occur at temperatures exceeding 5500°F, it is logical to examine the behavior of these correlations when extrapolated to higher temperature.

The next section explores some of the consequences of these extrapolations and Section 3.3 takes up the subject of material property variation in relation to data scatter.

3.2.3 Mass Loss at Temperatures Above 5500°F

The current single impact data base extends to 5500°F whereas calculations with nose-tip design codes (which include state of the art heating augmentation models) predict surface temperatures of the order of 7000°F (sample calculations will be presented in Section 4). It is therefore of great practical importance to have some guide for mass loss ratios at temperatures that are closer to those encountered in flight. To this end, the speculation that the correlations given in the preceeding section represent some measure of reality is examined in light of the predicted and expected mass loss ratio at high temperature.

Since the SoRI data covers the wider temperature range, the correlations using these data are more appropriate for this purpose, and in Figure 5 the predicted mass loss dependence on temperature (normalized by the mass loss at 4500°F) is shown, along with the data of Rubin, et al. (Reference 2). It is seen from Figure 5 that the predicted mass loss at 5500°F is nearly at a minimum with either correlation. For temperatures greater than 5500°., the correlation using compressive modulus increases at a greater rate with increasing temperature than the correlation with tensile modulus. Both correlations, as well as the one based on the Aerospace data, indicate that at sufficiently high temperatures, the trend of mass loss vs. temperature will be the opposite of that shown by the data at lower temperature. Formally, this behavior is a result of the fact that the elastic (and ultimate strength) properties approach zero at about 7000°F while the strain to failure remains finite (but large). Physical justification for this behavior is only qualitative, but very plausible. That is, simply, that there must be some temperature at which the material "strength" is reduced to a point where mass loss increases with temperature.

It is expected that the correlations of Section 3.2.2 will be found deficient in many details, for a number of reasons. However, if the mass loss ratio reverses its trend at temperatures typical of reentry, it is entirely possible that recession calculations will be seriously in error. This is a question that warrants further study and extended experimentation.

3.3 VARIABILITY OF MATERIAL PROPERTIES RELATED TO DATA SCATTER

In this section, the available statistical information of the variability of material properties (sample-sample) is combined with the mass loss correlations of Section 3.2 to obtain estimates of the contribution of these elements to scatter in the single impact data. Whereas the correlations are admittedly tentative and based on very sparse data, it is argued that the estimates herein are much more reliable.

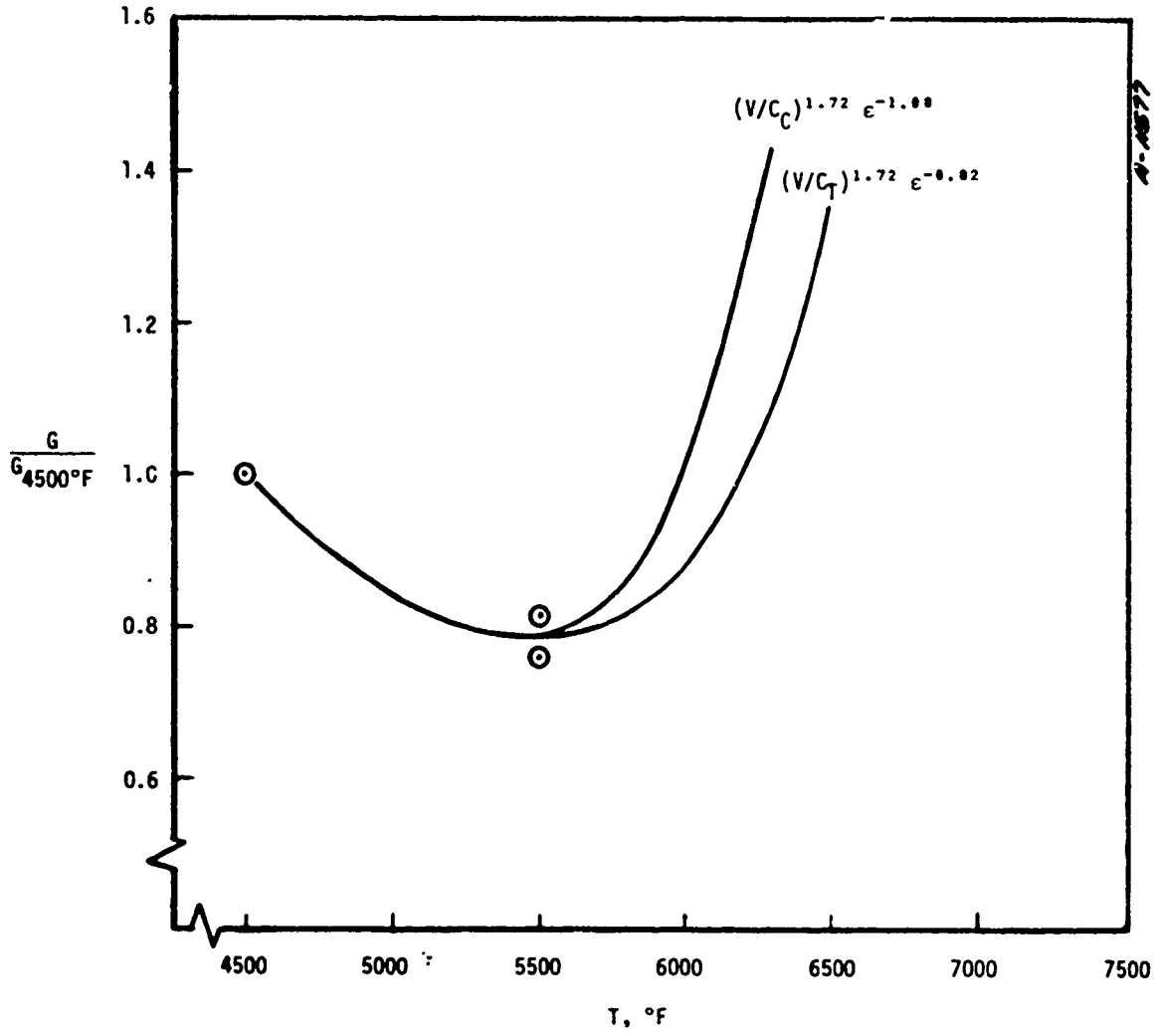

Figure 5. Comparison of extrapolated correlations at high temperature, data from Rubin and McClelland (Reference 2).

This follows from the dimensional necessity for material properties in the mass loss expression and the fact that subsequent calculations of variances only involve the exponents of the independent variables and the ratio of the standard deviation to the mean. Thus, even though the correlations may not have definitive form, it is most probable that other "strength" and "failure" properties are correlated with conventional material test results. It should also be pointed out that all exponents in the correlations are less than 2, hence there are no variables that are given excessive or unreasonable weight.

The data report by Starrett and Pears (Reference 17) gives tabulated values of the standard deviations obtained for the specimens tested. The Aerospace report (Reference 18) gives frequency histograms for the data, hence the values used here have been calculated from these distributions. The results are shown in Table 2 from which it is seen that elastic modulii have

$$0.05 \leq \frac{\sigma_E}{\mu_E} \leq 0\ 17$$

and that

$$0.03 \leq \frac{\sigma_\varepsilon}{\mu_\varepsilon} \leq 0.17$$

it is also seen from Table 2 that the trend of σ/μ is to increase with temperature, which is not surprising behavior.

Then using Equations (1) through (5), and the maximum values of the reported standard deviations, one finds that

$\frac{\sigma_G}{\mu_G} = 0.36$ with Equation (3) and the Aerospace data

$\frac{\sigma_G}{\mu_G} = 0.40$ for E_{AT} with Equation (4) and the SoRI data

$\frac{\sigma_G}{\mu_G} = 0.33$ for E_{AC} with Equation (5) and the SoRI data

Thus, the predicted standard deviation of mass loss due to random variation of the independent variables is estimated to be about ± 30 to ± 40 percent of the mean, which is consistent with the data

TABLE 2. STATISTICS OF MATERIAL PROPERTY TEST RESULTS

Temperature (°F)	Standard Deviation/Mean (Number of Samples)			Source
	E_{AT}	E_{AC}	ϵ	
1000	0.05(8)	0.12(8)	0.03(8)	Starrett and Pears (Reference 17)
2000	0.12(73)	0.12(8)	0.09(73)	
3000	0.10(55)	0.09(7)	0.13(55)	
3500	0.10(13)	0.17(7)	0.17(13)	
4000	0.11(18)		0.27(18)	
4500	0.15(4)		0.34(4)	
70	0.09(90)		0.11(71)	Channon (Reference 18)
3000			0.18(34)	

scatter band presented in Figure [illegible]nce, it is deduced that statistical variability of material properties is a major component of the observed scatter in single impact data and, it follows, contributes also to the scatter observed under conditions where the more complex phenomena resulting from coupled erosion/ablation effects are present.

The next section takes up the task of integrating these results with coupled effects predictions in order to identify the consequences and to make further deductions about the role certain elements play in these circumstances.

SECTION 4

COUPLED EROSION/ABLATION EFFECTS: PHENOMENOLOGY AND UNCERTAINTIES

Section 2 of this report discussed the morphology of coupled erosion/abaltion calculations and identified separate elements as possible contributors to uncertainties in such calculations. Subsequent sections have quantified and identified the causes of uncertainties (both in the trend and the scatter) associated with a single hypervelocity impact. This section combines these concepts in a study of the consequences in the more complex experimental situation where coupled erosion/ablation occurs.

A number of erosion testing facilities in current use subject a model to multiple particle impacts and simultaneous heating. Among these are the rocket sled, the dust tunnel and the rocket motor exhaust facilities (see Dahm, et al. (Reference 5)). However, a ballistic range experiment offers the closest simulation of reentry conditions in terms of matching the velocity, the particulate field concentration, the stagnation pressure and the thermochemistry involved in coupled effects. These considerations result in the choice of ballistic range data for the comparisons of this section.

Figure 6 is a comparison of the single impact correlation

$$G = AV^{1.72} \quad \text{(with } \pm 40 \text{ percent lines)}$$

with a selection of ballistic range data discussed by Berry, et al. (Reference 19). It is seen that the ballistic range data show a consistently larger mass loss than the single impact data as well as larger scatter, which is now of the order of a decade. In a ballistic range experiment, there is significant aerodynamic heating and some ablation mass loss during a test, even in a nonerosive environment (see the results of a tare shot on the AEDC Ballistic Range G reported by Jones (Reference 20)). It would appear to be a simple matter to subtract out this "ablation component" and thereby explain some of the difference in the trend of the two sets of data shown in Figure 6. As explained in Section 2, however, because of the way in which phenomena are coupled when erosion and ablation occur simultaneously, this is not possible. Thus, it is necessary to know the mass loss ratio before a calculation can be made. Since the total surface recession is the information obtained during the experiment, an unbiased erosion mass loss

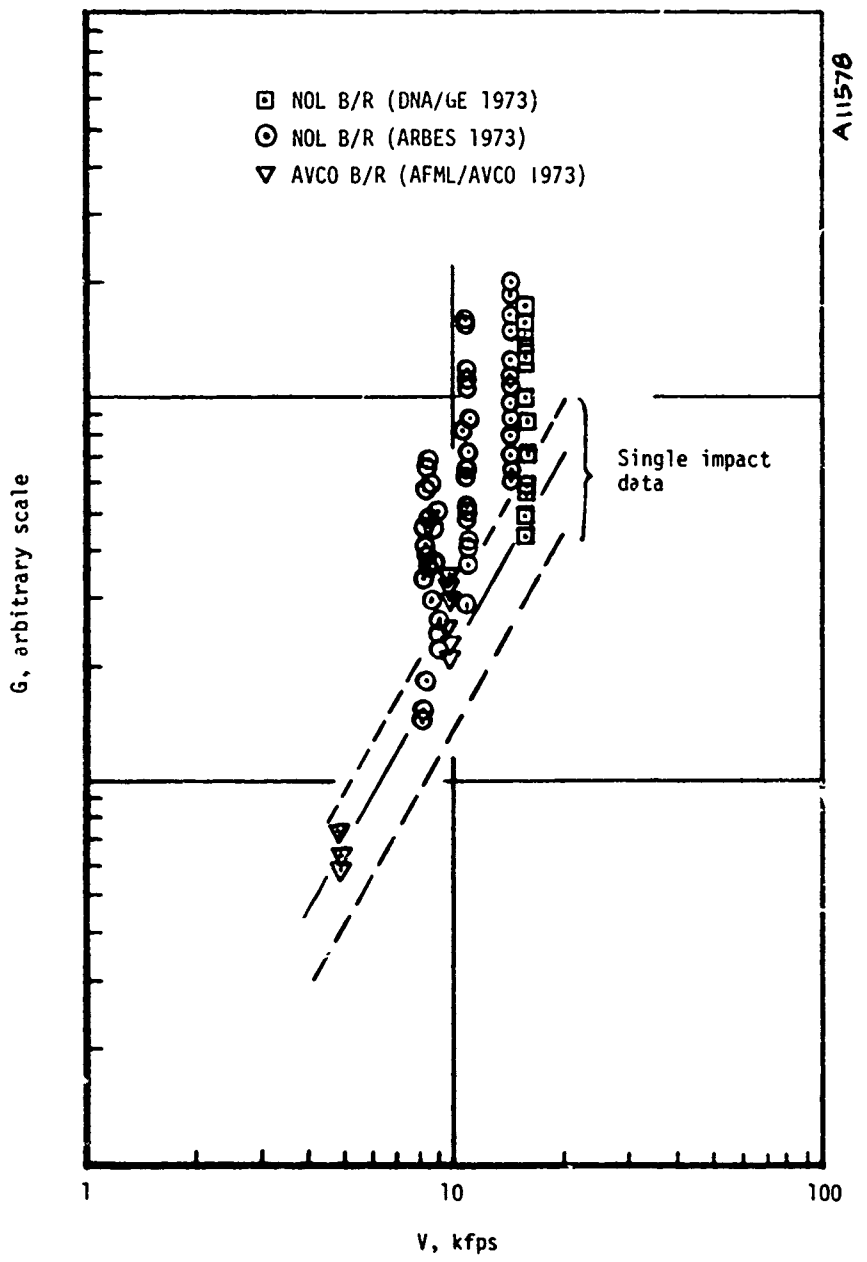

Figure 6. Comparison of single impact correlation and uncertainty with ballistic range and other data selected by Berry, et al. (Reference 19).

component is not the result of the experiment even though it has been sometimes reported as such (or at least without the distinction noted). The obvious way to deal with this situation is to assume G (e.g., from single impact experiments), make a calculation of the coupled erosion/ablation recession, and compare the predicted surface recession and surface temperature with those observed in the ballistic range. Unfortunately, this introduces additional uncertainties and sources of errors associated with the modeling and prediction of each additional phenomenon. Referring to Figure 1, if obscuration, for example, is relevant to a particular ballistic range shot, then the uncertainties in modeling this effect further contribute to errors in predicted recession. Similarly, if there is an intrinsically statistical factor involved with the phenomenon (and obscuration is certainly of this type) there are bound to be added variations in the measured recession. Other areas of concern are associated with the surface temperature as it affects mass loss through coupling with the material response and with the heating model because of its contribution of the resulting temperature and because it determines the magnitude of the ablation component of recession.

In order to quantify individually some of these effects, a modified version of the Aerotherm Erosion Shape (EROS) computer code was created, with which it is possible to selectively uncouple certain aspects of the calculation. This also makes possible a clearer understainding of the role played by various elements in the overall scheme. The following section describes this pilot code and the results of its application to ballistic range experiments.

4.1 DIAGNOSTIC VERSION OF THE EROS CODE

With an appropriate choice of ballistic range experiments, it is possible to reduce the number (or at least the magnitude of the effect) of some of the elements in the morphology of a coupled calculation. Thus, if the ballistic range dust environment is considered, shock layer effects are much better defined. Furthermore, debris shielding is probably not relevant to flight, hence the low field concentration experiments in the extended AEDC Range G (440 feet) are the most useful in that this problem is thereby bypassed. With these restrictions, the problems under investigation are reduced to questions about coupling between the ablation, surface energy balance (SURFEB), augmented heating (AH) and single impact mass loss (G_s) elements shown in Figure 1.

The necessary decoupling in the code is accomplished by creating options that place switches in two places, one disconnects the erosion mass loss rate ($\dot{m}_E$) from SURFEB and another disables the heating augmentation, AH. By selection of G_s (which is input to the code) the surface temperature effect on material response can be adjusted. These options allow for

the investigation of a number of important areas and provide the basis for answers to some basic questions. For example, since the mechanical mass loss removes high temperature nose-tip material, the implication that follows from a surface energy balance is that the surface temperature should be reduced. This would result in lower ablation mass loss and lower or higher resistance to erosion depending on the functional form of $G_s(T)$. However, an additional effect of erosion is to augment the convective heating of the surface, resulting in an entirely opposite trend for the surface temperature, the thermochemical ablation component and the effect on mechanical mass loss ($G_s(T)$). It is seen, then, that deletion of $\dot{m}_E$ in SURFEB while retaining AH will result in a surface temperature that is an upper limit for that achievable at a given flight condition. On the other hand, with $\dot{m}_E$ but without AH, the output of SURFEB will be a temperature (among other things such as the ablation component of mass loss) that is a lower limit for the same conditions. A clarification of the interplay of these factors, the quantification of the limits and an identification of the consequences relevant to improving coupled erosion/ablation predictions are the objectives sought by using the decoupled code.

Hence, the options in the modified (for this study) version of EROS facilitate the isolation of the important elements, the identification of the dominant physical processes and the ability to track through the morphology the effect of an uncertainty associated with an individual element.

Further simplifying assumptions that have been made in the present study are that there is no shape change, that steady state is achieved, and that continuum erosion is realistic. It is seen from Figure 1 that, in general, this simplifies an additional coupling between the nose-tip geometry and the shock layer shape which is then only a function of the trajectory. In the present study, it has also been assumed that there is no particle deceleration, breakup or demise. The other important aspect of the surface geometry, its roughness, does change with time, depending on the growth of surface roughness due to turbulent heating and roughening due to impacts. Craters are assumed hemispherical and a crater roughness is calculated accordingly, as

$$k_c = \left(\frac{G_s}{4}\frac{\rho_p}{\rho_t}\right)^{1/3} d_p \qquad (6)$$

Two erosion related heating augmentation mechanisms are operative. One is the "stirring" augmented heat transfer correlation developed by Science Applications Inc. (SAI) and

given by Courtney, et al. (Reference 21). This correlation is combined with an angle dependence to give a laminar, erosion augmented "free stream" Stanton number distribution as

$$C_{HLS} = 0.093 \left\{ \frac{w}{\rho_\infty} (1 + G) \right\}^{0.317} \sin^2\theta \qquad (7)$$

where w = mass density of erosive field (liquid water content)

ρ_∞ = free stream mass density

θ = angle between the surface tangent and free stream velocity vectors

In this study, a convenient measure of the relative magnitude of the resulting heat transfer is used. It is defined as

$$FKLS = \frac{\rho_\infty u_\infty C_{HLS}}{\rho_e u_e C_{HL}} \qquad (8)$$

where C_{HL} = Stanton number for laminar flow without erosion (based on the boundary layer edge conditions and the intrinsic roughness)

The other erosion related heating augmentation mechanism is that due to surface roughness induced by cratering. In this case, it is applied in both the laminar and the turbulent regimes (but through appropriately different correlations). In the laminar region, k_c is compared to k_i (the intrinsic roughness, k_i = 0.0004 in. for ATJ-S), and the larger of the two is used in the PANT rough wall laminar heating augmentation correlation, as described by Rafinejad, et al. (Reference 22). For the present study, the relative magnitude of this effect is measured by FKLR, which is

$$FKLR = \frac{C_{HLR}}{C_{HL}} \qquad (9)$$

where C_{HLR} = Stanton number for laminar rough wall heat transfer

Then, to calculate the laminar heat transfer coefficient, the larger of FKLS and FKLR is used.

In the transitional and turbulent parts of the flow field, the larger of k_c and k_i is used in the heat transfer correlations for these regions, except that the scallop roughness is also involved, as described by Rafinejad, et al. (Reference 22). Also shown in Reference 22 is the expression used to calculate a composite turbulent heat transfer coefficient from the laminar and turbulent components.

The matrix of solutions that were studied with this modified version of EROS is as shown in Table 3. It is seen from Table 3 that all possible combinations of on/off heating augmentation and on/off $\dot{m}_E$ in SURFEB are covered. It should also be emphasized that heating augmentation here refers exclusively to that due to erosion since k_c and C_{HLS} are set to zero by this option.

As discussed previously, the other important aspect of the present study is the mass loss expression and its temperature dependence. The choices in this case, therefore, are related to the previous findings as well as current practice. Thus, the expression for G_s given in Section 3.1 is one of the cases studied (see Table 4). Also considered were the expressions that result from the estimated $\pm\sigma$ uncertainty levels for the single impact data. In order to investigate the consequences of temperature dependent ATJ-S mass loss, a composite expression was constructed. This is simply an empirical fit to the data of Rubin and McClelland (Reference 2) of the form

$$G = AV^{1.72}\,(T/4350)^{-0.784}$$

for

$$T > 4350°R$$

which is compared to the data in Figure 7. This form was chosen over those shown on Figure 5 because, although any extrapolation beyond 5500°F is conjectural at present (including the above), the $\pm\sigma$ uncertainty bands bracket any of the extrapolations, if it is assumed that the temperature is less than 7000°R.

The remaining mass loss expression was chosen as the one developed by Nardo, et al. (Reference 23) for carbon/carbon 2-2-3. This is

$$G = BV^{1.8}\,T^{0.2}\,d_p^{-0.3}\,(\sin\theta)^{1.2}$$

and is of interest in the present context because of the positive power on temperature and the fact that carbon/carbon composite materials are an important class of RV materials.

Table 4 summarizes these relationships, which, when combined with the list of options given in Table 3, give a total of 20 cases. Only 14 of these were considered because the trends observed in some cases are duplicated in others. Thus the combinations between

$$\left\{\begin{matrix}\text{A00}\\ \text{B00}\\ \text{C00}\end{matrix}\right\}\left\{\begin{matrix}\text{PS}\\ \text{MS}\end{matrix}\right\}$$

TABLE 3. MATRIX OF OPTIONS FOR COUPLED EROSION/ABLATION STUDY VERSION OF EROS COMPUTER CODE

Option	Internal Logic	Comments
A00	No heating augmentation, no $\dot{m}_E$ in SURFEB	Surface temperature and thermo-chemical ablation will be the same as in clear air
B00	No heating augmentation with $\dot{m}_E$ in SURFEB	Demonstrates lowest continuum-steady temperature to be expected
C00	With heating augmentation, no $\dot{m}_E$ in SURFEB	Analog to two physical situations: (1) eroded material leaving at room temperature or (2) upper limit (steady state) to achievable surface temperature
D00	With heating augmentation with $\dot{m}_E$ in SURFEB	Complete current continuum-steady state modeling
SURFEB		Surface energy balance surboutine
$\dot{m}_E$		Erosion mass loss rate
FKLS or FKLR		Heating augmentation factors

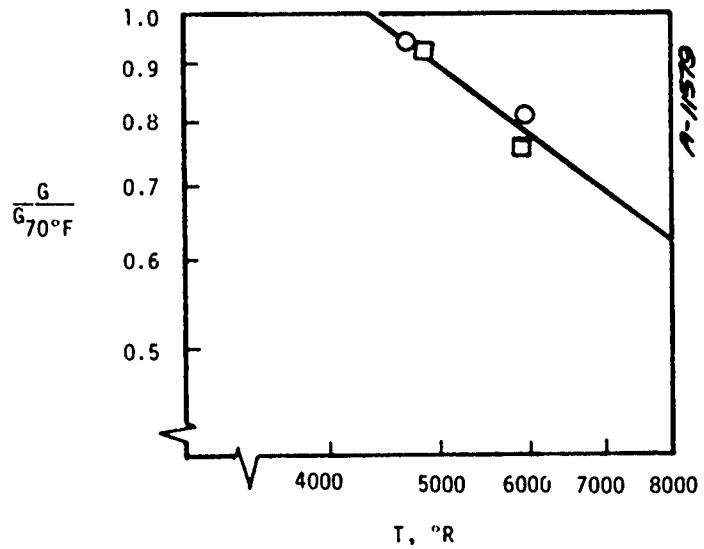

Figure 7. Comparison of empirical fit with the data of Rubin and McClelland (Reference 2).

TABLE 4. SUMMARY OF MASS LOSS EXPRESSIONS USED IN CALCULATIONS

Designation	Mass Loss Expression	Material
AA	$G = AV^{1.72} (\sin \theta)^{0.6}$ for $T < 4350°R$ $G = AV^{1.72} (T/4350)^{-0.784} (\sin \theta)^{0.6}$ for $T \geq 4350°R$	ATJ-S
BB	$G = AV^{1.72} (\sin \theta)^{0.6}$	ATJ-S
PS	$G = 1.4\ AV^{1.72} (\sin \theta)^{0.6}$	ATJ-S
MS	$G = 0.6\ AV^{1.72} (\sin \theta)^{0.6}$	ATJ-S
CC	$G = BV^{1.8} T^{0.2} d_p^{-0.3} (\sin \theta)^{1.2}$	C/C 2-2-3

were not investigated, because to a large extent that would mean duplication of most features of the cases:

$$\left\{\begin{matrix} A00 \\ B00 \\ C00 \end{matrix}\right\} \{BB\}$$

It should also be noted that the angle dependence for impact into ATJ-S has been assumed proportional to

$$(\sin \theta)^{0.6}$$

which is consistent with the deductions of Benjamin (Reference 9). In the study of single impacts reported in Section 3, angle effects were excluded because of a much greater deficiency in theoretical results than for many other aspects of the phenomena. Here, however, because of its obvious relevance to the completeness of the calculations, the empirical angle dependence factor has been used.

4.2 BALLISTIC RANGE RESULTS

For reasons outlined earlier, a ballistic range experiment with low dust field concentration was chosen.* In order to provide a comparison with recent data, the environment of Shot No. 4149 from the recent SAMSO/Aerospace series reported by Jones (Reference 20) was chosen. The relevant environmental parameters for this experiment are shown on Figure 8.

The general nature of the predicted stagnation point surface recession rate is shown in Figure 9 for ATJ-S and $G = KV^{1.72}$ with the fully coupled code (case D00*BB). It is seen that the erosion component ($\dot{S}_E$) is approximately 75 percent of the total ($\dot{S}_T$). The ablation component calculated using augmented heating ($\dot{S}_A$) is also seen to be about 2.8 times the tare shot ablation component. Thus, as indicated previously, subtracting the tare shot ablation from $\dot{S}_T$ would result in an erosion component that is about 22 percent too large.

Figure 10 shows the results of the calculations for ATJ-S assuming mass loss decreases with temperature (case D00*AA). As expected the total recession is less than when G_s is independent of temperature. Of interest is the observation that the ablation component calculated using augmented heating is practically the same as that of the previous case, which makes its contribution proportionally larger; $\dot{S}_A \approx 0.38\ \dot{S}_T$.

---

*Although the erosion field is dust, particles of unity specific gravity were used in these calculations. The effect is to yield smaller crater depths and snorter obscuration times than expected for dust.

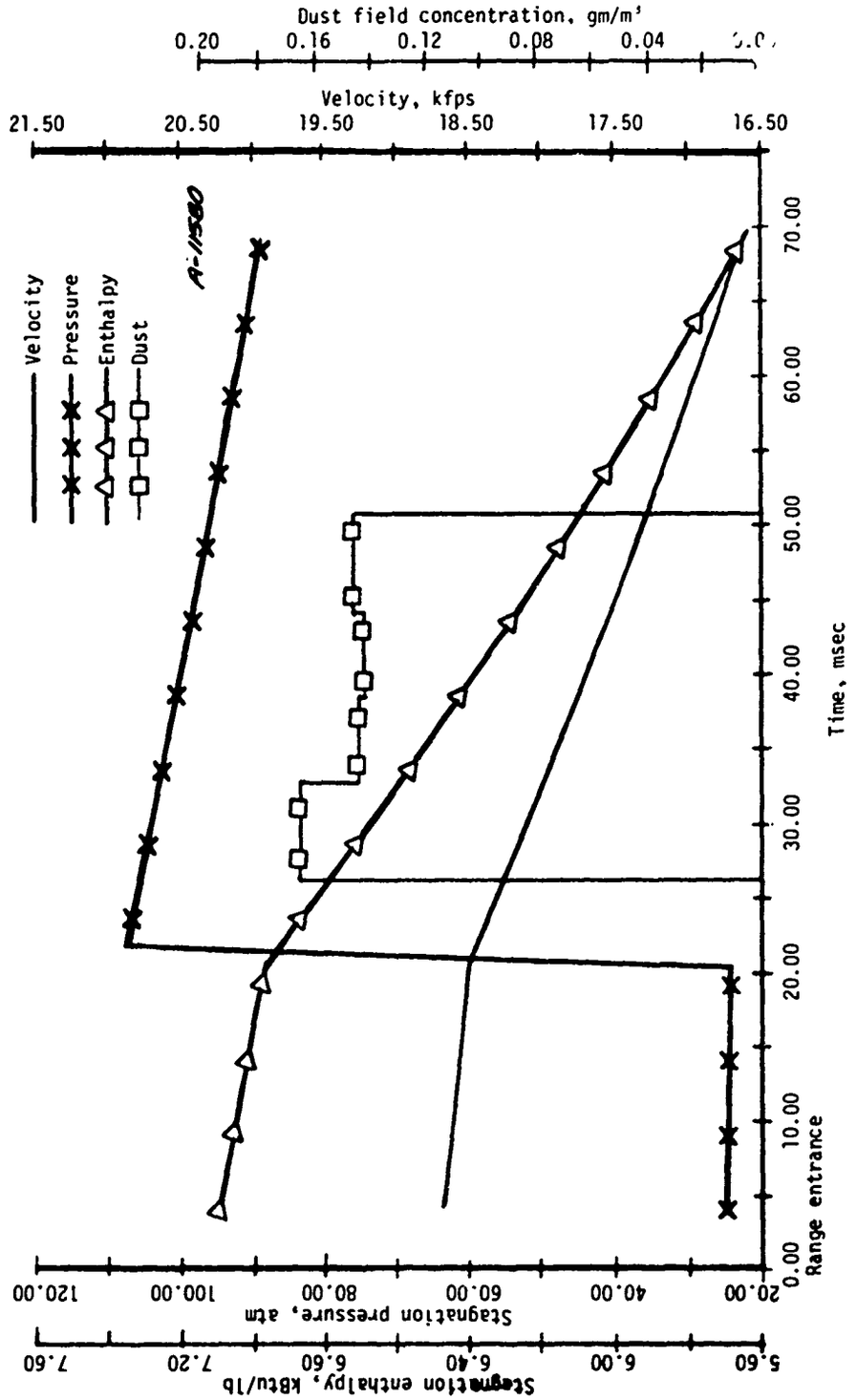

Figure 8. Ballistic range environment from Jones (Reference 20).

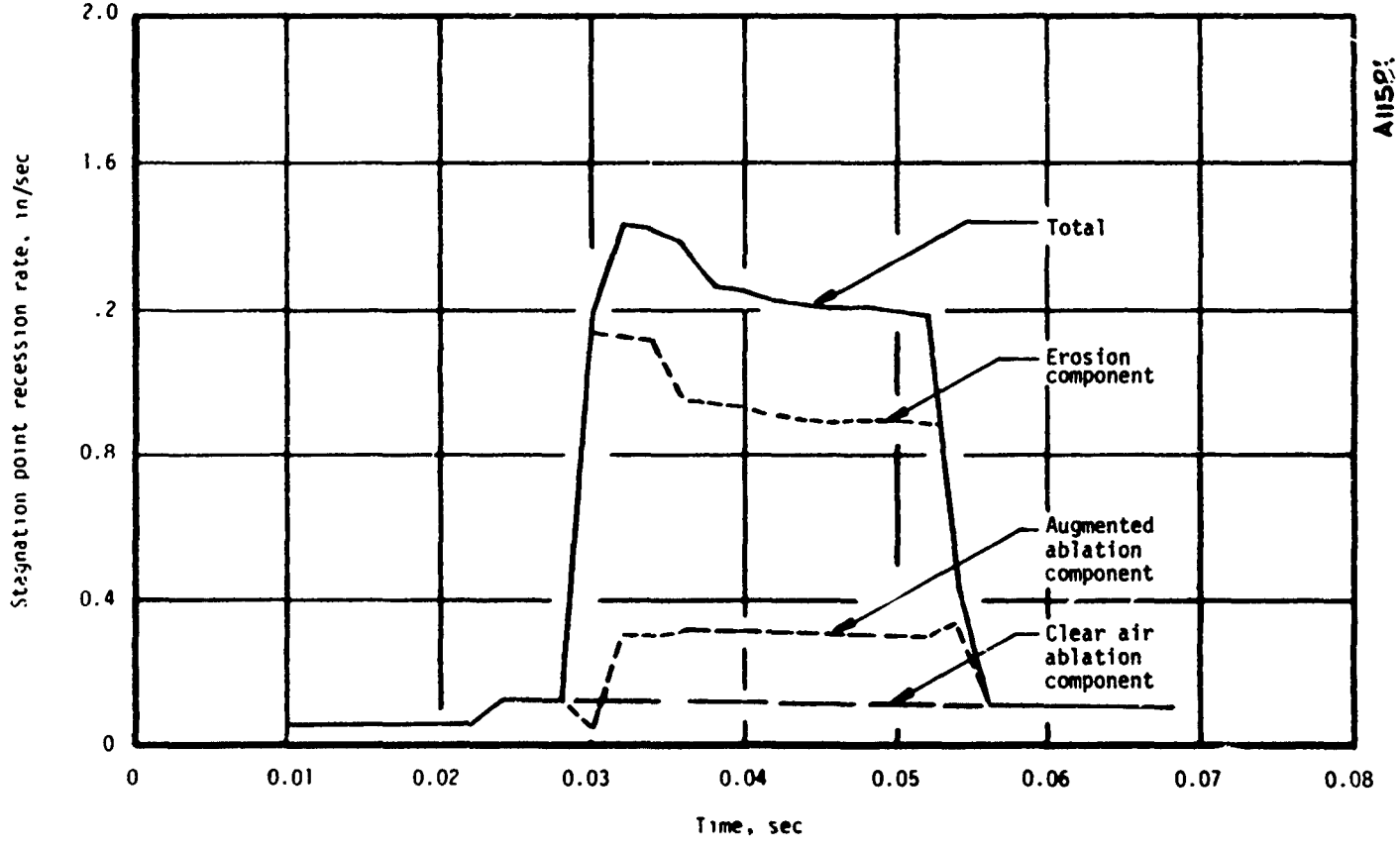

Figure 9. Comparison of components of surface recession rate in ballistic range; ATJ-S, fully coupled, mass loss independent of temperature (case D00*BB).

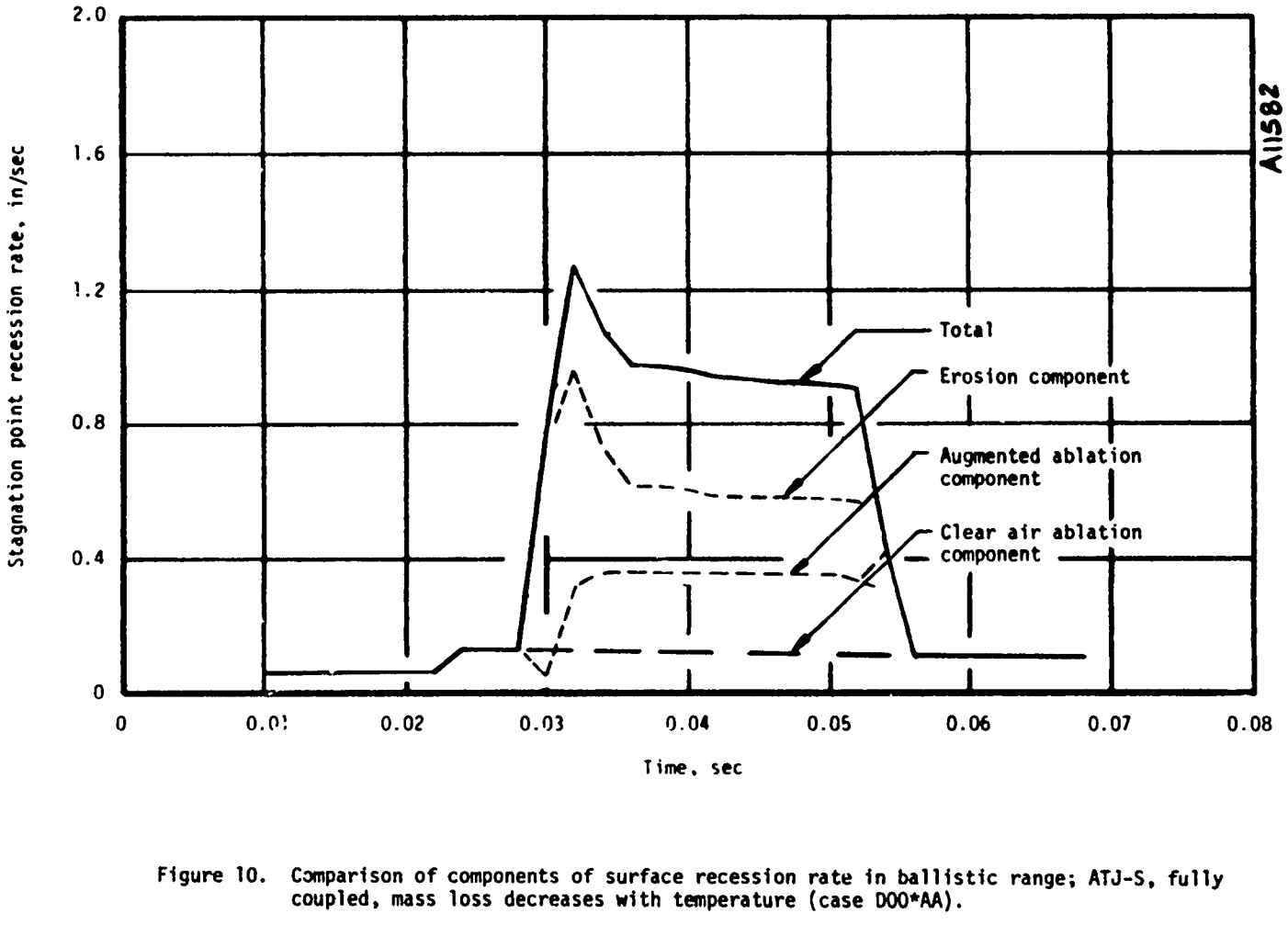

Figure 10. Comparison of components of surface recession rate in ballistic range; ATJ-S, fully coupled, mass loss decreases with temperature (case D00*AA).

The subtlety of the fully coupled problem is well illustrated by comparison of these two cases, because $\dot{S}_A$ with G_s (V,T) is actually slightly larger than $\dot{S}_A$ with $G_s(V)$, a result contrary to intuition at first glance. The explanation is as follows: mass loss tends to decrease T (as a result of SURFEB) which tends to reduce $\dot{S}_A$, but mass loss also induces augmented heating which tends to increase T and $\dot{S}_A$. Thus, there is a certain balance between the effect on $\dot{S}_A$ of the two phenomena. The decrease of G with T between cases D00*AA and D00*BB is just enough to slightly change the ratio of these two effects. The numerical results for a typical time are summarized in Table 5, which also shows that the laminar "stirring" augmentation factor (Equation (8)), FKLS, and the laminar roughness augmentation factor (Equation (9)), FKLR, are nearly equal, with FKLR just slightly larger. This is the general level and the usual comparison between these two factors that is found in the ballistic range for the particular cloud density considered. but not in other situations, as will be shown.

shown in Table 5 are the stagnation point results from the uncoupled cases at the same time step. It is seen that augmented heating is a major factor because it very nearly compensates for what would otherwise be (note cases B00*) a much reduced surface temperature. There are other important features of Table 5, such as the effect of augmented heating without $\dot{m}_E$ which results in the largest $\dot{S}_A$. This gives an upper limit of about $\dot{S}_A \approx 0.44\ \dot{S}_T$ in a ballistic range experiment (at the range pressure of 230 mmHg and cloud density of 0.15 gm/m^3).

However, from the point of view of uncertainties in a given shape change prediction, the consequences of an uncertainty in G_s are of prime importance. The simplest way to examine this issue is to make a calculation with $G_s = \mu_G + \sigma_G$ and $G_s = \mu_G - \sigma_G$.

The results of these computations are shown in Figure 11 which is a comparison of $\dot{S}_T$ and $\dot{S}_A$ for the two cases of (D00*PS and D00*MS). It is seen that there results a $\pm$27 percent uncertainty in total stagnation point recession rate. The resulting uncertainty in $\dot{S}_A$ is due to the effect on crater roughness which is proportional to $G^{1/3}$; it amounts to $\pm$10 percent. In these calculations, crater roughness gives an augmentation factor (FKLR) slightly larger than FKLS; but the functional dependence on G_s of each of these factors is essentially identical.

Thus, in a ballistic range experiment the net result of a $\pm$40 percent uncertainty in the result of a single impact translates into a $\pm$27 percent uncertainty in predicted stagnation point recession rate. Specifically, this is an estimate of the expected variation of $\dot{S}_T$ in a ballistic range for a number of shots with material samples chosen at random but all

TABLE 5. BALLISTIC RANGE RESULTS, COMPARISON OF TEMPERATURE DEPENDENT MASS LOSS EXPRESSIONS, EFFECTS OF $\dot{m}_E$ AND AH, TIME = 0.04 SECOND

Case		T, °R	Recession Rates (in/sec)			Mass Loss G	FKLR	FKLS
			$\dot{S}_T$	$\dot{S}_E$	$\dot{S}_A$			
$G_s(V,T)$	D00*AA	7707	0.94	0.59	0.35	36	3.79	3.28
$G_s(V)$	D00*BB	7512	1.25	0.93	0.32	57	3.96	3.76
No $\dot{m}_E$, no AH	A00*AA	7933	0.70	0.58	0.12	35	1.0	0.00
With $\dot{m}_E$, no AH	B00*AA	4765	0.93	0.87	0.06	53	1.0	0.00
No $\dot{m}_E$, with AH	C00*AA	7996	1.03	0.58	0.45	35	3.79	3.26
No $\dot{m}_E$, no AH	A00*BB	7933	1.05	0.93	0.12	57	1.0	0.00
With $\dot{m}_E$, no AH	B00*BB	4588	0.98	0.93	0.05	57	1.0	0.00
No $\dot{m}_E$, with AH	C00*BB	7997	1.41	0.93	0.48	57	3.98	3.78

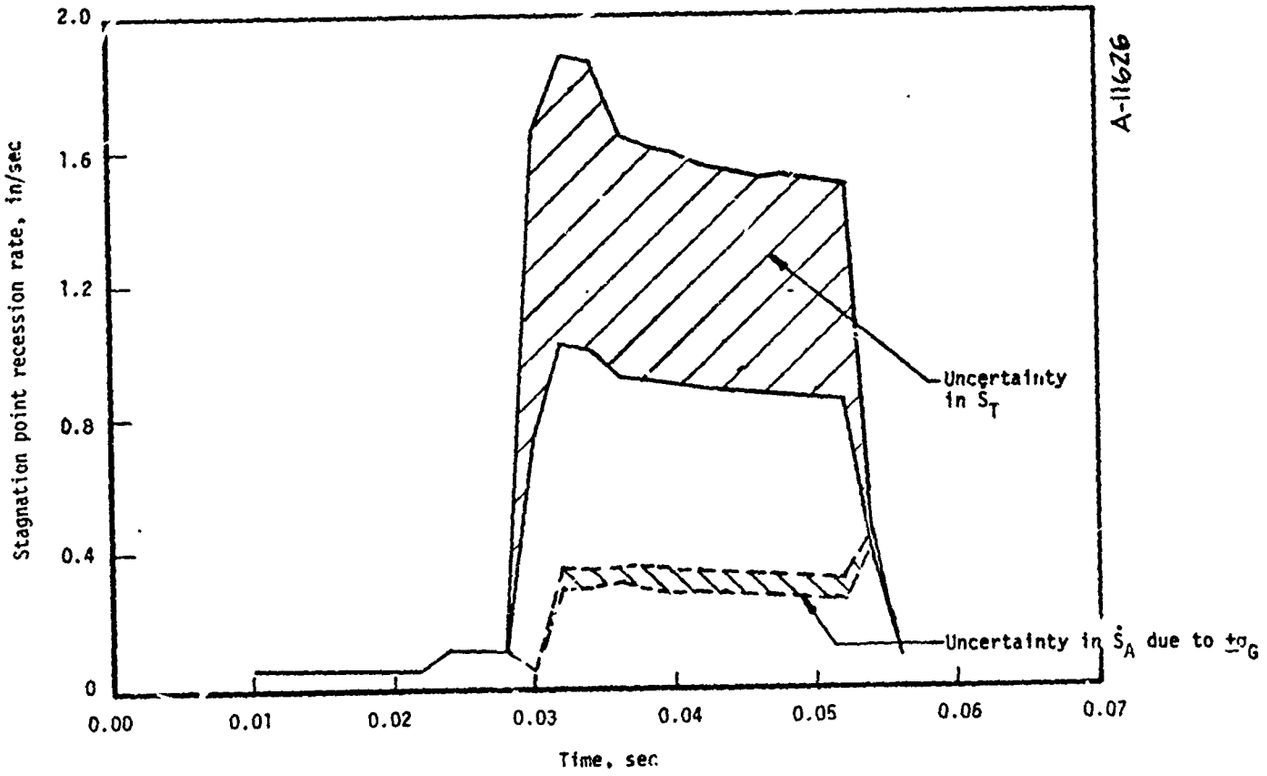

Figure 11. Comparison of recession components with $\pm\sigma$ uncertainty in G_S; ballistic range, ATJ-S, fully coupled code (D00*PS, D00*MS).

other parameters held constant. In a single ballistic range experiment, there are, in reality, fairly large uncertainties of other kinds. Thus, for Shot 4149, Jones (Reference 20) reports an experimental uncertainty in impacted mass from ±16 percent to ±22 percent and an uncertainty in total mass loss of ±14 percent to ±25 percent. The present calculations have also neglected shock layer effects and assumed that an impact does not predamage the surface, which in terms of the experimental unknowns, translate into additional uncertainties.

At present, it is not possible to precisely quantify all of these uncertainties but it does become fairly clear that the accumulated effect is consistent with the observed scatter. In summary of these matters, the following list of sources of uncertainties, magnitudes and comments are suggested as representative:

Source	Magnitude	Comments
Material properties	±27% in $\dot{S}_T$	Relevant in comparing different samples
Impacted mass	±20% in $\dot{S}_T$	Intrinsic to BR instrumentation
Measured mass loss	±20%	Intrinsic to BR instrumentation
Shock layer effects	-20%	Without considering breakup effects
Predamage	+20%	Guess based on influence of material properties
Augmented heating	±10% in $\dot{S}_T$	Based on uncertainties in this effect other than these related to σ_G

It is seen that not all of these uncertainties are of the same kind, since some are intrinsic to a given experiment, some relate to comparison of repeated experiments and others express unknowns associated with modeling of phenomena that are in principle less uncertain. Thus, it cannot be expected that the above can be simply added to total the net scatter, but these estimates do explain why data, plotted as G vs. V without regard to any other consideration, show large discrepancies. As an example, a rough estimate may be obtained by using Equation (2) with unity exponents (i.e., the sum of the squares rule). Taking the above estimates for the magnitudes of the component uncertainties and an additional 33 percent error in $\dot{S}_T$ due to neglect of the ablation component, the square root of the sum of the squares becomes

$$\frac{\sigma_{\dot{S}_T}}{\dot{S}_T} = 0.60$$

Hence, with a 90 percent confidence limit arbitrarily taken at $\pm 2\sigma$, an overall scatter band of the order of a factor of 4 would be predicted, which is seen to be entirely consistent with the scatter of the experimental results shown in Figure 6. These arguments are not proposed as definitive, but rather to make the point that a significant reduction in the overall scatter of coupled erosion/ablation data can be realized if a more complete analysis of the relevant phenomena is undertaken in the process of data reduction.

To complete this discussion of the ballistic range results, the components of surface recession rates for carbon/carbon 2-2-3 are shown on Figure 12. These results generally show the same trend as do those for graphite. Some differences in detail exist, such as the somewhat larger erosion component shown in Figure 12 when compared to that shown in Figure 9. In this case it is also possible to make a comparison with the data of Jones (Reference 20), which is shown in Figure 13. The brackets on the data in Figure 13 indicate typical maximum values obtained from the profile drawings reported by Jones (Reference 20). Since the model turns in flight, each laser station gives a different view of a very rough surface. In spite of this aspect of the profile data, it is more convenient than the mass loss data for the present purposes. Figure 13 shows that there is reasonable agreement between the prediction and the data.

With this study of uncertainties associated with data derived from ground test facilities as background, the following section examines some of the consequences in flight situations, first for a SAMS flight and then for a trajectory typical of reentry.

4.3 FLIGHT RESULTS AND IMPLICATIONS

This section is concerned with the flight consequences of some of the issues of the previous section. The purpose here, is to translate some of the known uncertainties into assessments of flight predictions and to gain insight into differences that should be taken into account in the process.

The first case considered is the SAMS 7 flight experiment. This is a relatively low velocity (8500 fps) launch through a low altitude storm system, as shown by the velocity and cloud concentration vs. altitude distributions in Figure 14. The maximum particle diameter encountered on this trajectory is 1355 μm, and the average value is about 1000 μm in the dense part of the weather.

Generally, the interaction of components in the morphology of the coupled calculation is about the same as for a ballistic range experiment with some differences in detail. The

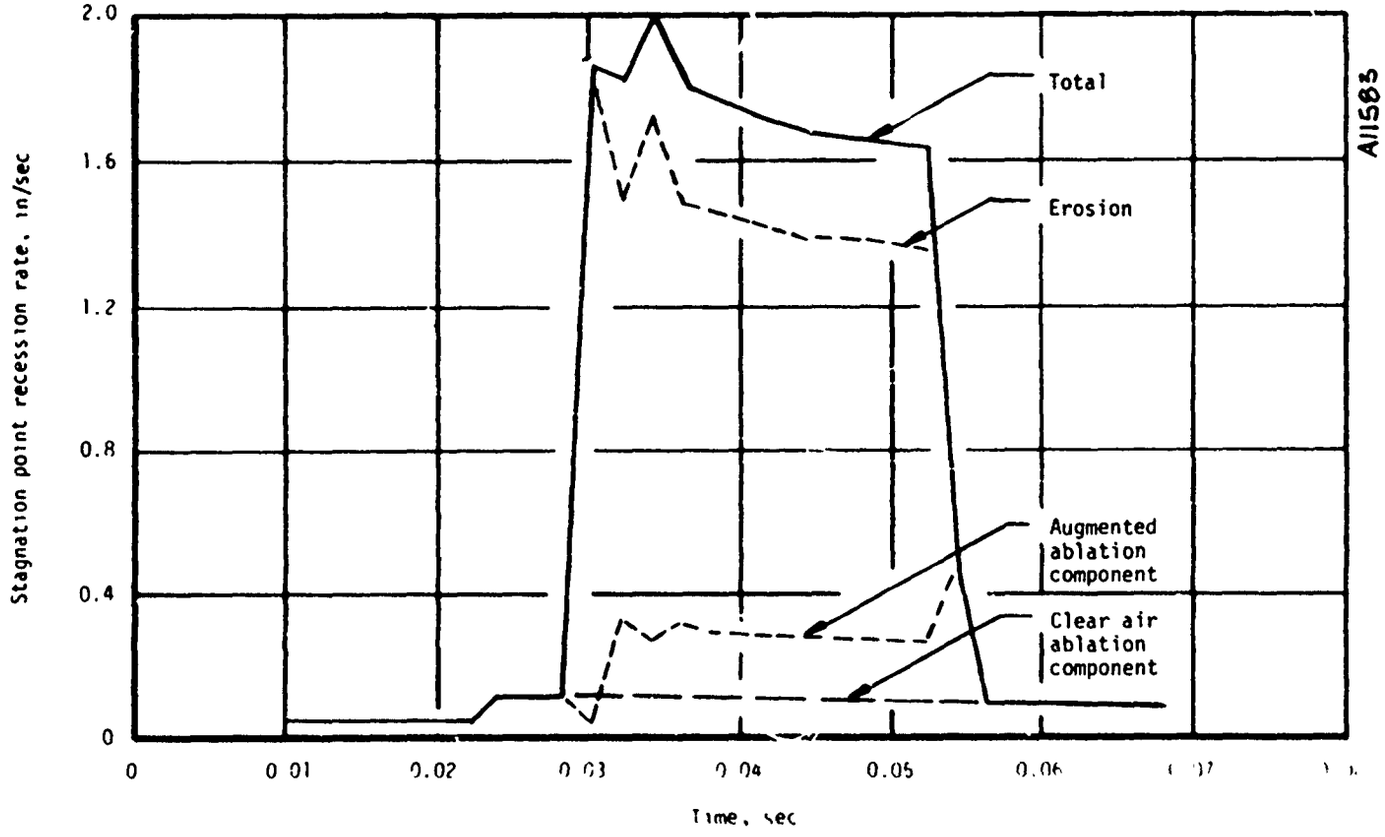

Figure 12. Comparison of components of surface recession rate in ballistic range; C/C 2-2-3 (case D00*CC).

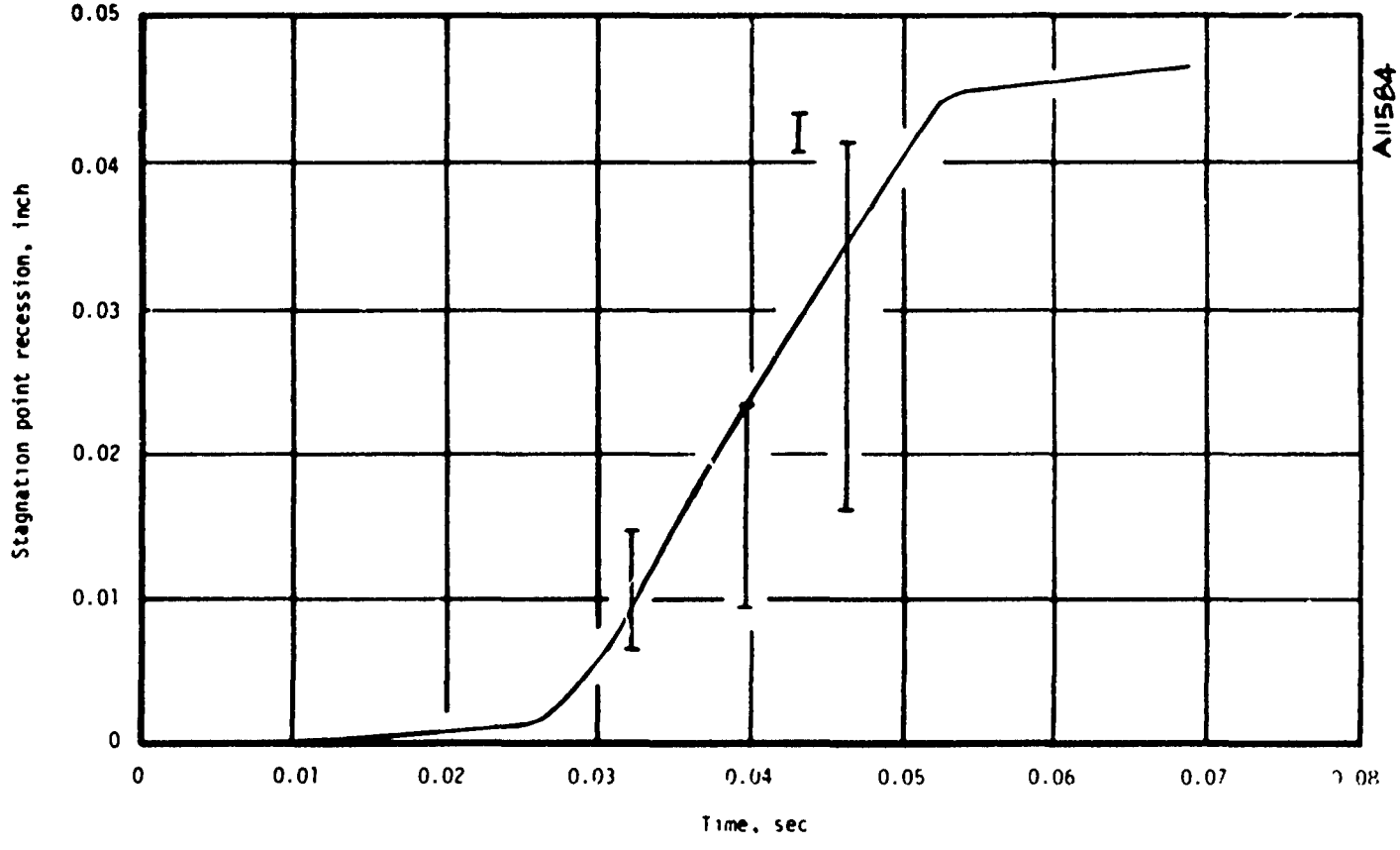

Figure 13. Comparison of ballistic range data with predicted stagnation point recession, C/C 2-2-3.

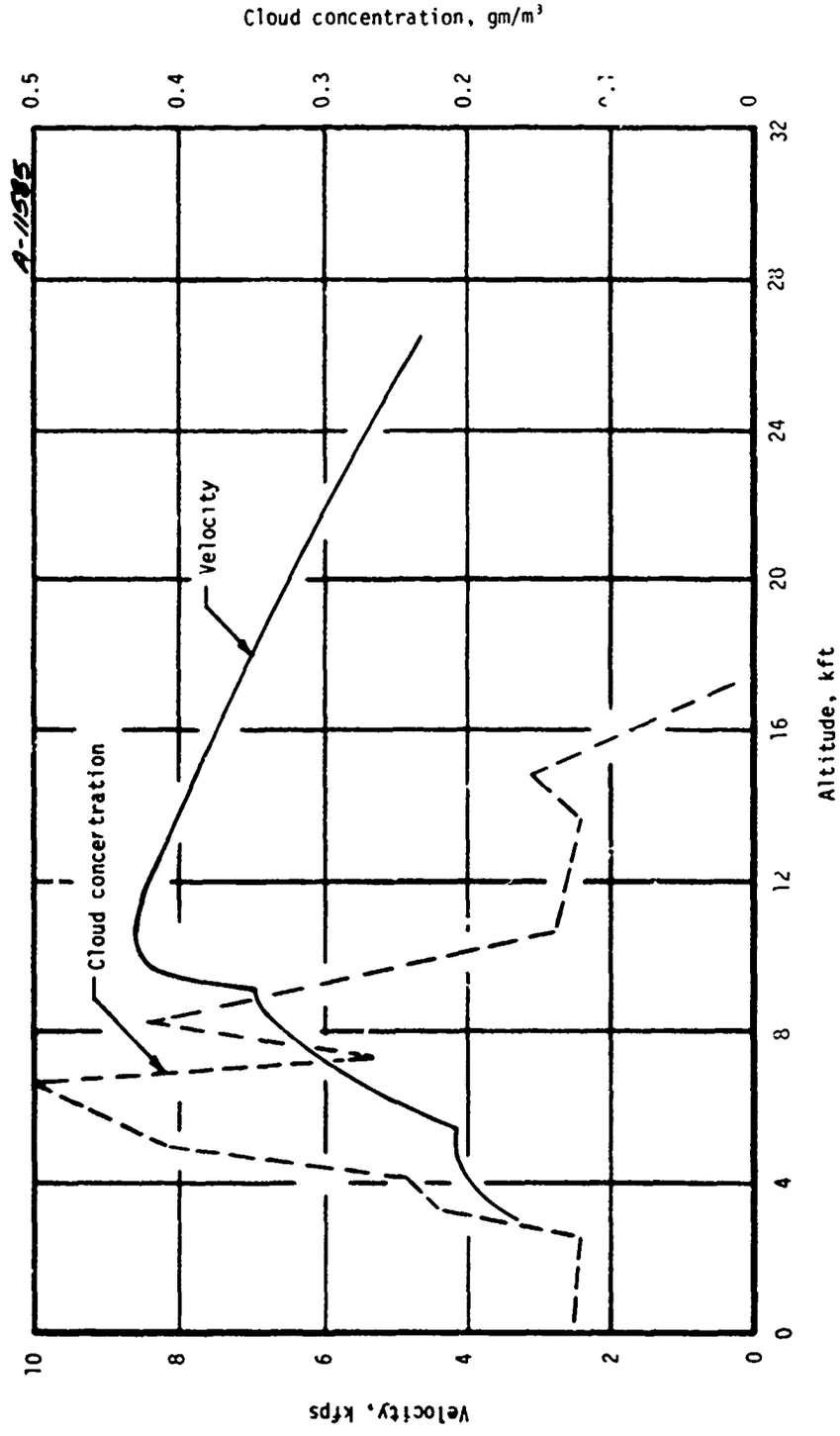

Figure 14. Vehicle velocity and cloud concentration distributions for the SAMS 7 flight.

effect of $\dot{m}_E$ in SURFEB is qualitatively the same as in the ballistic range environment when the difference in velocity is taken into account. The effect of heating augmentation is also similar in that its contribution to the surface energy balance nearly compensates for the energy lost through $\dot{m}_E$, resulting in a surface temperature almost equal to the clear air value.

Figure 15 shows the components of the stagnation point recession rate predicted with the fully coupled code. It is seen that the ablation component (with augmented heat transfer) is of the order of 40 percent of the total at about 6.7 seconds into the flight (where $\dot{S}_T$ is a maximum). This is a slightly larger fraction than found in the ballistic range experiments, and is due to the comparatively low velocity in the SAMS flight. The largest of the augmentation factors in this case is FKLS = 7.2, compared to FKLR = 5.2. Thus, at high field concentration and low velocity the erosion stirring augmentation mechanism dominates crater roughness. It will be shown below that this trend continues when reentry flights are considered.

The trajectory and the weather for the reentry flight are shown in Figure 16. The weather is Profile No. 388 which has a weather severity index of 20 and average particle diameters from 250 μm to 1000 μm. As shown on Figure 16, the cloud is encountered at 16.1 seconds into the flight and step changes in the liquid water content occur at 17.1, 17.8, 18.6 and 19.0 seconds.

One of the issues discussed previously (in Section 3.2.3), was extrapolation of G_s to temperatures higher than those of the data base. The reentry flight relevance of this question is examined here by first presenting the results calculated with the decoupled version of EROS. Shown on Figure 17 are the stagnation point wall temperature histories predicted by the four options of the uncoupled version of EROS. The material for the calculations shown in Figure 17 is carbon/carbon 2-2-3, with the G_s given in Table 4. These temperature histories, from the various options, are typical of those found for graphite with the mass loss expressions shown in Table 4. The trends discussed earlier are seen to be accentuated in flight, because of the high velocity and (in this case) the relatively heavy weather. Thus, with heating augmentation disabled, the mechanical mass loss removal rate contribution to SURFEB results in a very low surface temperature. With heating augmentation, this effect is nearly balanced and the resulting surface temperature is only slightly less than its clear air value. Therefore, in flight as well as in the ballistic range environments, heating augmentation is a major factor in maintaining high surface temperatures.

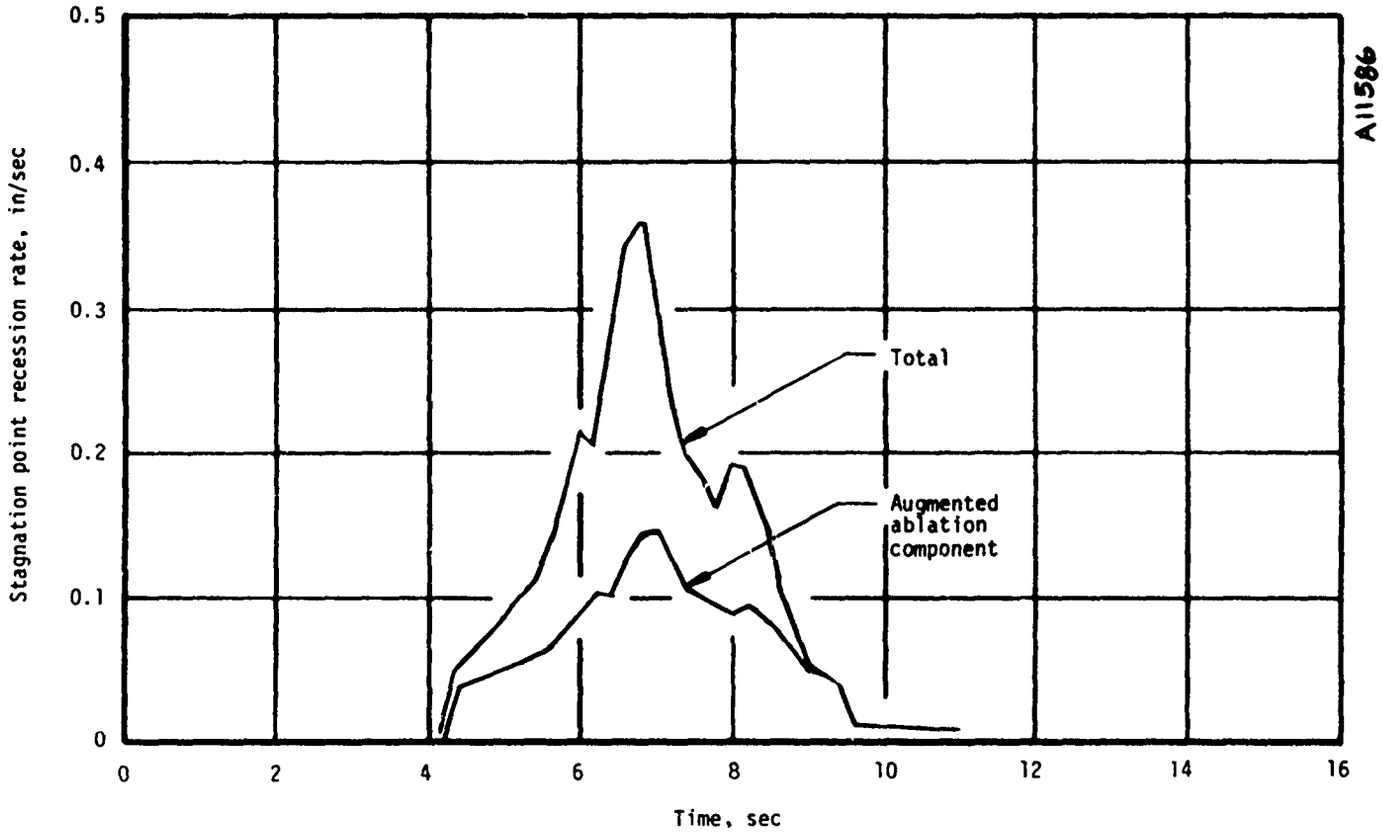

Figure 15. Comparison of the recession rate components for the SAMS 7 flight, ATJ-S with $G_s(V,T)$.

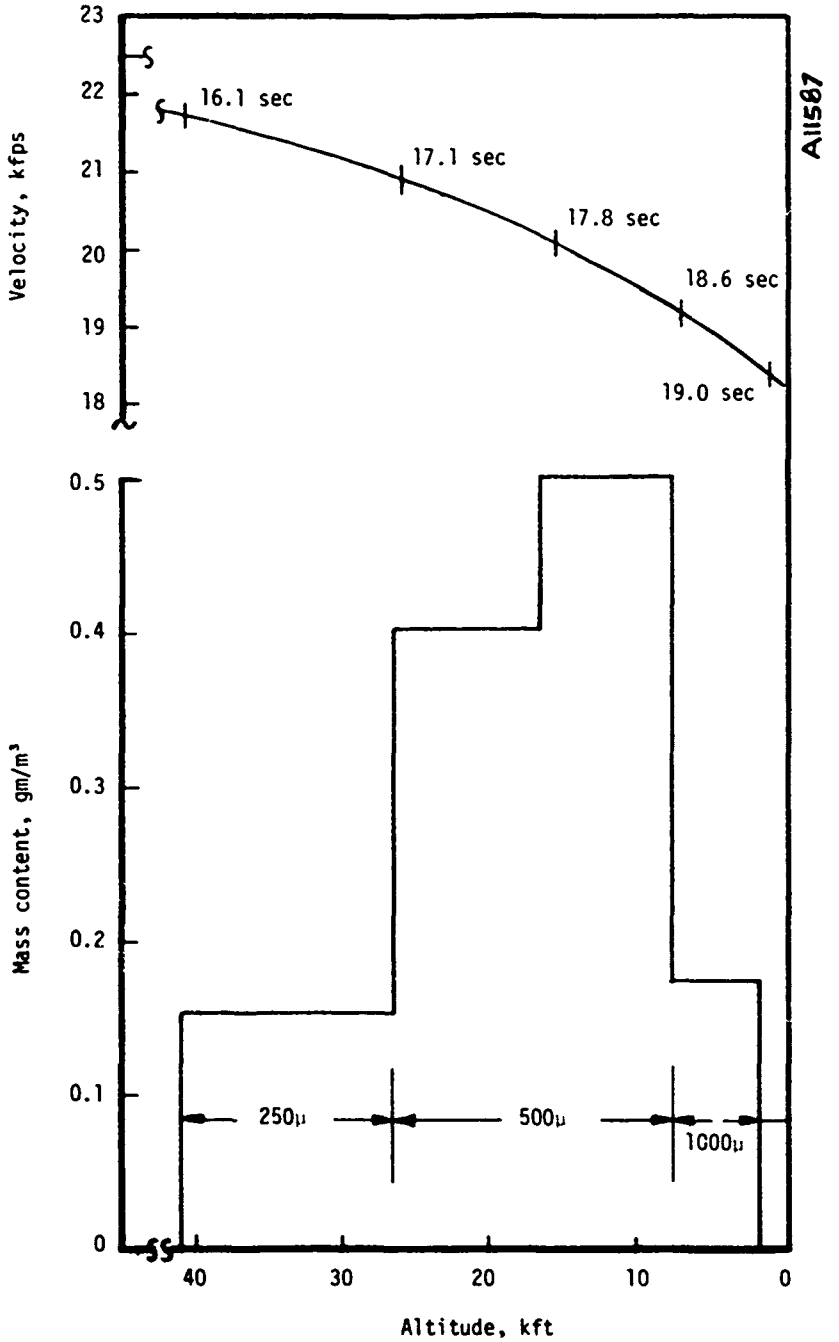

Figure 16. Trajectory and weather distribution for reentry flight.

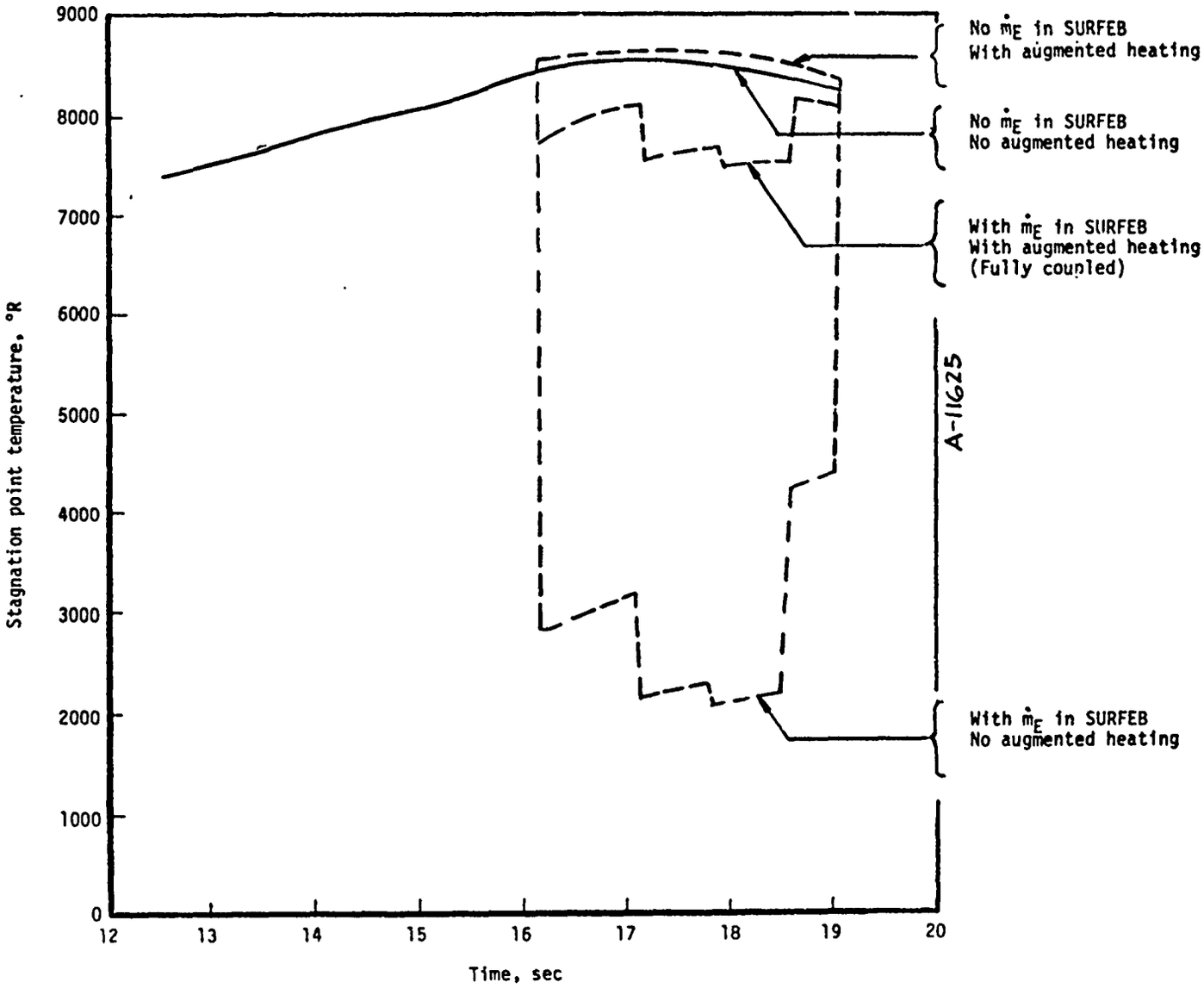

Figure 17. Stagnation point wall temperature histories for C/C 2-2-3 predicted by uncoupled options of EROS; reentry weather flight.

The behavior of G_s at temperatures in the neighborhood of 7000°R is therefore of consequence in overall flight performance, as shown in Figure 18, which compares total surfact recession rates using $G_s(V)$ and $G_s(V,T)$ for graphtie. It is clear from Figure 18 that the difference between the calculated recession rates resulting from these mass loss expressions is signficant, being of the order of 40 percent.

A comparison of these results is shown below, for a time 18 seconds into flight at the stagnation point, and for ATJ-S

T_w, °R	in/sec $\dot{S}_T$	$\dot{S}_E$	$\dot{S}_A$	G	FKLR	FKLS
7689	5.40	4.57	0.83	$G_s(V) = 71$	4.89	11.91
7994	3.77	2.86	0.91	$G_s(V,T) = 44$	4.71	10.3'

It is evident that the wall temperature is high enough that the choice of mass loss expression is very important, especially if it should be found that the trend of G vs. T reverses about 6000°R as suggested by the correlation of Section 3.2.3. Furthermore, these high surface temperatures are a result of the stirring augmentation factor, FKLS, which is relatively insensitive to the particular form of G_s. The surface temperature is, therefore, expected to be in the range indicated above regardless of possible changes in G_s. Since the ablation component (with heating augmentation) is relatively insensitive to changes in G_s, the major impact appears in the erosion component.

In summary of this section, it is shown that an uncertainty in mass loss, when traced through the morphology of coupled erosion/ablation calculations, has a major impact on the prediction of nosetip performance.

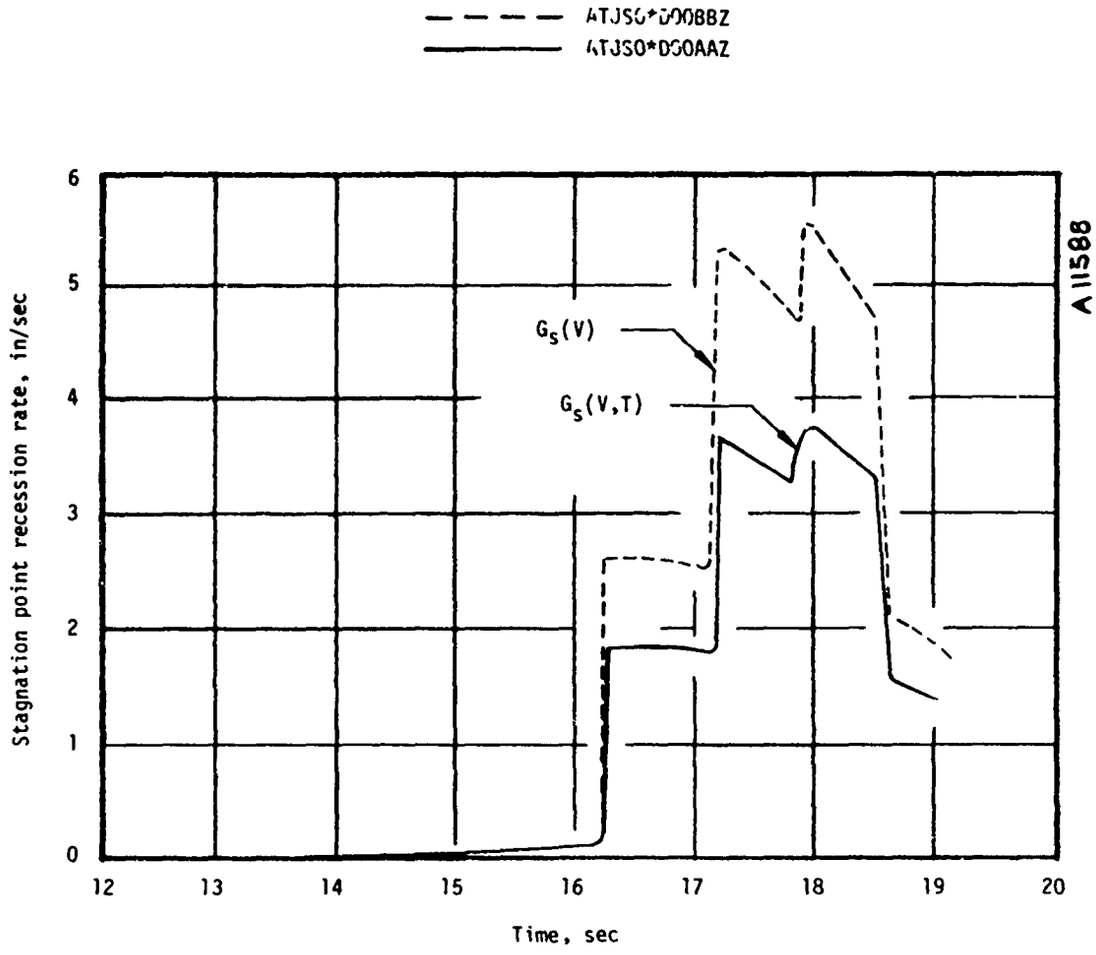

Figure 18. Comparison of recession rates during reentry using G(V) and G(V,T) for ATJ-S reentry flight.

SECTION 5

CONCLUSIONS AND RECOMMENDATIONS

The complex morphology of coupled erosion/ablation shape change (Section 2) requires that elucidation of the overall consequences of data scatter and uncertainties associated with one aspect of the process depends on knowledge (or the lack of it, i.e., additional uncertainties) of the other elements in the phenomena and their interactions. Therefore, the problem was studied by reducing it to its primary elements and interactions, determining the magnitude and cause of uncertainties in separate elements and relating these results to overall uncertainties in coupled erosion/ablation recession rates.

The process that is basic to erosion is single impact mass loss. Since correlation of single impact mass loss data for ATJ-S using velocity as the only independent variable gives an uncertainty of the order of ±40 percent, too large to be explained by known experimental errors, a search for other relevant variables was undertaken. Dimensional analysis indicates the need to include material strength and failure related properties in single impact mass loss expressions. A study of available theoretical results, comparison of recent high temperature single impact data with the known dependence of mechanical properties of ATJ-S on temperature, and plausible intuitive arguments resulted in the choice of elastic modulus and strain to failure as the most probable additional independent variables for a generalized ATJ-S mass loss expression.

With the resulting single impact mass loss expression of Section 3.2, it was shown that it is possible to give a reasonable explanation for the scatter observed in single impact data in that known sample to sample variations of elastic modulus and strain to failure are sufficient to account for most of it.

The generalized single impact mass loss expression was also shown to fit recent data which is for the temperature range from 4500°F to 5500°F, and to extrapolate beyond that range with a trend of mass loss increasing with temperature. This is the reverse of the mass loss vs. temperature trend observed at low temperature, but is consistent with intuitive arguments.

The consequences of these results for the origin and the magnitude of single impact mass loss uncertainties were evaluated for the environment of the ballistic range where the presence of coupled erosion/ablation effects makes the erosion mass loss component an implicit function of other elements. The circumstances chosen were those of a low concentration dust field in the AEDC Ballistic Range G. This situation was studied because it further simplifies the considerations, insofar as shock layer/particle interactions, shape change effects, obscuration effects and particle/material response uncertainties (compared to snow) are reduced as much as possible. With these simplifications, coupled erosion/ablation effects are reduced to the essential elements of (1) the erosion mass loss rate, (2) the erosion augmented heating effects, (3) the surface energy balance, and (4) the ablation mass loss rate. The coupling and interaction of these elements determines the total surface recession rate, which reflects the consequences of an uncertainty in one (or more) of the elements.

With a version of the Aerotherm EROsion Shape (EROS) computer code modified to allow the determination of the magnitude of the effect of mechanical mass loss on augmented heating and the ablation mass loss rate and vice versa, it was found that in a low field concentration ballistic range experiment:

1. A $\pm$40 percent uncertainty in single impact mass loss results in $\pm$27 percent uncertainty in total recession rate.
2. The ablation mass loss rate component is typically of the order of 30 percent of the total recession.
3. Augmented convection is the controlling factor in the surface energy balance which determines the wall temperature and consequently the ablation component.
4. Temperature extrapolation of single impact mass loss has a significant influence on calculated recession rate.

These results were combined with other available information to explain the large scatter observed in ballistic range data when it is correlated as mass loss vs. velocity (as the only independent variable). As summarized in Section 3, component uncertainties of the order of $\pm$20 percent to $\pm$30 percent in total recession rate are associated with:

1. Uncertainties in single impact mass loss
2. Experimental uncertainties in the ballistic range
3. Ablation component of mass loss

4. Heating augmentation uncertainties

5. Shock layer/particle interactions.

These component uncertainties are not independent or additive in their effect on total mass loss in a coupled erosion/ablation environment. However, the inclusion of the parameters relevant to these phenomena is identifiable as a primary requirement for the reduction of ballistic range data.

Two flight cases, SAMS and ICBM, were examined by the same method to determine the effect of the uncertainties in these circumstances. Generally, the results were as given above and of particular importance is the finding that for an ICBM flight through weather, the role of heating augmentation is important in maintaining the surface temperature and providing a corresponding influence on mechanical mass loss rate.

In view of the needs established by these results, a combined ballistic range-single impact test plan is recommended and described in detail in the Appendix. The present results suggest that single impact and ballistic range experiments can be designed to be complementary. The parameters that need to be matched in order for this to be feasible have been calculated using current methodology and can be implemented with relative ease. Additional consideration of the variables involved in the prediction of coupled effects in a ballistic range experiment leads to a test matrix in which the model surface temperature is constant (predicted by current modeling) over a range of field concentrations and pressures. Within the constraints of existing experimental apparatus and techniques, these proposed test conditions provide a close approach to an optimum. This approach to optimum conditions is in terms of:

1. A minimum number of phenomena involved in the coupled erosion/ablation mass loss process

2. A procedure for experimental determination of single impact mass loss at conditions as close as possible to those of the ballistic range

3. Data analysis of ballistic range results using Item 2 above and state of the art coupled erosion/ablation technology.

The objectives of this test plan and the associated analytical methodology are:

1. To reduce sources of errors and uncertainties related to sample to sample differences in material response to hypervelocity impact insofar as ballistic range/single impact comparisons are concerned

2. To provide a basis for discrimination of single vs. multiple impact effects and other phenomena related to the state of the nosetip material

3. To allow the comparison and evaluation of erosion augmented heating models.

These objectives are of major importance in improving coupled erosion/ablation prediction methods, developing better simulation of flight environments and increasing the efficiency of erosion resistance screening of materials.

REFERENCES

1. Sullivan, R. J., "Dust Erosion Behavior of Materials at Hypervelocity," Part II (U), AFML-TR-70-186, Part II, December 1972 (CONFIDENTIAL).

2. Rubin, L. and McClelland, J., "The Influence of Temperature on Hypervelocity Erosion of Graphite," Aerospace Corporation, El Segundo, California. Paper presented in Fourth International Conference on Rain Erosion and Associated Phenomena in Meiroburg, Federal German Republic, May 1974.

3. Personal communication with Louis Rubin of Aerospace Corporation, El Segundo, California, unpublished data.

4. Reinecke, W., McKay, W. and Waldman, G., "Aspects of High Speed Rain, Oil, and Dust Erosion of Advanced Materials (U)," AVCO Corporation, Wilmington, Massachusetts, November 1974, AFML-TR-74-170.

5. Dahm, T. J., Cooper, L., Powars, C. A., and Jackson, M. D., "Assessment and Extension of Erosion Testing Capabilities," Aerotherm Report 74-103, Acurex/Aerotherm, Mountain View, California, May 1974.

6. Graham, M., et al., "Development of the Particle Impact Test Facility," Effects Technology, Incorporated, Santa Barbara, California, presented at the 25th Meeting of the Aeroballistic Range Association, Naval Ordnance Laboratory, October 1974.

7. Graham, M., Effects Technology Incorporated, Santa Barbara, California, personal communication.

8. Rubin, L., Aerospace Corporation, El Segundo, California, personal communication.

9. Benjamin, A. S., "Hypersonic Erosion Facilities Comparison and Rain, Dust and Ice Correlation (U)," AFML-TR-73-233.

10. Rae, W. J., in High Velocity Impact Phenomena, R. Kinslow, Ed., Academic Press, NY, 1970.

11. Greszczuk, L. B., "Response of Isotropic and Composite Materials to Particle Impact," Foreign Object Impact Damage to Composites, ASTM STP568, American Society for Testing Materials, 1975.

12. Timoshenko, S. and Goodier, J. N., Theory of Elasticity, McGraw-Hill, New York, 1951.

13. Walsh, J. M. and Sedgwick, R. T., "Studies of Erosion and Impact Resistance of ABM Materials," Systems, Science, and Software Report SS-R-74-2399, La Jolla, California, November 1974.

14. Gurtman, G., personal communication, Systems, Science and Software, Inc., La Jolla, California.

15. Kreyenhagen, K. N., Wagner, M. H., and Goerke, W. S., "Direct Impact Effects in Hypersonic Erosion," SAMSO-TR-73-339, August 1973.

16. Rosenblatt, M., personal communication, California Research and Technology, Woodland Hills, California.

17. Starrett, H. S. and Pears, C. D., "Probable and Average Properties of ATJ-S(WS) Graphite," AFML-TR-73-14, Volume 1, February 1973.

18. Channon, S. L., "Reentry Materials Handbook," Aerospace Corporation, TOR-1001 (S2855-20)-3, December 1968.

19. Berry, R. A., Lee, K. C., Kriebel, A. R., Nardo, C. T., and Wool, M. R., "Investigation of Erosion Mechanics on Reentry Materials (U)," Acurex/Aerotherm Report TR-75-139, March 1975, (SECRET).

20. Jones, G. R., "SAMSO/Aerospace Snow/Dust Erosion Test (U)," Preliminary Data Package," Project V41G-34A, AEDC-ARO Incorporated, February 1975 (SECRET).

21. Courtney, J. F., Wenger, R. S., and Binder, J. D., "Nosetip Material and Geometry Effects on Aerodynamic Heating in Erosion Environments," DNA 3481F, August 1974.

22. Rafinejad, D. and Derbidge, T. C., "Computer User's Manual: Nosetip Shape Change Including Erosion (EROS)," Aerotherm Division/Acurex Corporation, June 1975.

23. Nardo, C. T., Wool, M. R., and Clark, K., "Assessment of an Alternative Material for Minuteman RV Nosetip Application (U)," Acurex/Aerotherm Report TM-75-60, February 1975, (SECRET).

APPENDIX

A TEST PLAN FOR COUPLED EROSION/ABLATION EXPERIMENTS

TABLE OF CONTENTS FOR THE APPENDIX

A.1 INTRODUCTION

The results of the study of coupled erosion/ablation effects, data and uncertainties given in Section 4 indicate a number of problem areas associated with use of data from ballistic range experiments. It was shown, for example, that the existence of erosion augmented heat and mass transfer in a ballistic range contributes significantly to the total mass loss rate and surface temperature and makes the erosion mass loss component an implicit function of the total (observed) recession. Examples of a method for circumventing this difficulty were given in Sections 3 and 4. This method is based on mass loss correlations developed from single impact data; used in conjunction with coupled code calculations to obtain recession predictions directly comparable with the results of ballistic range experiments. In this method, the results of the two experiments are compared on a basis that includes an accounting for the additional phenomena present in the ballistic range. With appropriate selection of the ballistic range environment, the number and complexity of additional effects can be reduced, leading to fewer uncertainties in the calculation and a better framework for the comparisons.

An experimental approach that includes this method of data analysis and is adjusted to minimize possible sources of errors is therefore suggested as a means of improving the state of the art of coupled erosion/ablation predictions. Expected improvements are in the areas of (1) coupled erosion/ablation modeling, (2) better understanding of how to simulate flight environments, and (3) increases in the efficiency of screening of materials for erosion resistance.

With the background and the details on coupled effects provided by Section 4, the next section identifies those parameters that can be made common between the two experimental methods and the reasons for doing so. Section A.3 discusses the choice of materials, test samples and procedures that are designed to reduce the related uncertainties. Experimental procedures relevant to improving some aspects of the desired similitude among flight-single impact-ballistic range tests are discussed in Section A.4. The recommended test matrix and data analysis program are given in Sections A.5 and A.6.

A.2 PARAMETERS IN BALLISTIC RANGE AND SINGLE IMPACT EXPERIMENTS

In this section, the similitude parameters that are relatively easily made common between a ballistic range (BR) and a single impact (SI) experiment are discussed in the context of the requirements for reconciliation of the data. The experimental variables of major

importance are fairly obvious; for the particle(s) they are mass density, diameter and impact velocity; for the nosetip material they are those that describe its thermal and mechanical state. The detailed reasons for the particular choices suggested herein are somewhat more involved and are discussed below.

A.2.1 Impacting Particle(s)

The proposed tests would use 300 μm dust particles (glass beads with mass density $\rho_p \approx$ 3.3 gm/cm^3) for both SI and BR experiments. This size particle can be easily launched in a SI facility and has been used in BR experiments in the AEDC Range G (see Jones (Reference A1)). From the point of view of an erosive environment encounter by a reentry vehicle, dust may be improbable, but according to the cratering calculations of Kreyenhagen, et al. (Reference A2) there is little difference between dust and water impact response.* The major reason for this choice, however, is based on the phenomenology in a ballistic range, where a shock layer around the model must be accounted for. Modeling of passage through a shock layer is simply much easier for a dust particle than for rain, ice or snow. Since it seems improbable that a dust particle can break up during (or after) shock layer traverse, this mode of particle demise is eliminated. It appears necessary only to account for particle deceleration, and this seems fairly well in hand. There remain some uncertainties about shock layer transit by dust involving possible transient effects associated with the time required for drag to build up (as observed for water drops by Jaffe (Reference A3)) and particle ablation. Nevertheless, in describing its shock layer interaction, dust must be regarded as having the smallest uncertainty.

The other area of concern in matching the particle variables between a SI and the BR is the impact velocity. Generally, available SI data are in the 12 kfps range (see Table 1 of Section 3.1) but, according to Graham (Reference A4), it is currently possible to accelerate a 300 μm particle to 18 kfps. This easily provides a range of overlap with that available in the AEDC Range G (see Jones (Reference A1)). In fact, the velocity range from about 10 kfps to 18 kfps is useful for determination of the velocity extrapolation of mass loss (necessary to perhaps 25 kfps) and for evaluation of possible velocity effects on heating augmentation.

---

*Simple estimates of crater size accounting for particle size and density suggest snow and dust to be nearly equivalent at the same cloud density. Surface obscuration times are also nearly equivalent.

A.2.2 Target State

At present, it appears that the state of the nosetip material can be adequately matched between SI and BR experiments if the surface temperatures are nearly equal, although some qualifications to this statement must be noted.

Surface temperature gradients have two effects on erosion: (1) they influence materials stresses near the surface, and (2) cause material property gradients to exist over the regions influenced by the impact due to material property variations with temperature. Thus, temperature gradients are probably important in terms of erosion behavior, but probably secondary to surface temperature level effects. At present there is no conclusive evidence that aerodynamic pressure on a nosetip is sufficient to prestress the material enough to influence hypervelocity impact events. According to Rosenblatt (Reference A6), it is possible to assess the effect of prestressing the target (either by imposing a normal surface stress or a thermal stress), using current codes for the numerical solution of impact. This should be done, and if any significant effects are found, appropriate experiments should be considered.

If the dust field concentration in the BR is high, it will result in impact rates sufficient to bring about several model surface obscurations. When this occurs, the result of an impact on a location previously cratered may give greater mass loss than on an undamaged location. This circumstance cannot be easily duplicated in SI tests, but can be avoided in the BR. The data of Jones (Reference A1) show that it is feasible to make recession measurements in the BR when the obscuration is low. There are some differences in the method of calculating obscuration (see Benjamin (Reference A5) and Benjamin, et al. (Reference A6)), however, taking the values quoted for the SAMSO/Aerospace tests by Jones (Reference A1), it is judged that field concentrations at 18 kfps of the order of 0.10 gm/m^3, with 300 μm particles, are sufficient to avoid this effect.

Note, however, that the uncertainty in the experimental magnitude of eroded/ablated material increases on a percentage basis as the obscuration decreases. A surface obscuration of unity implies on the order of one crater depth of material removed – several mils of material. For these small eroded depths, the "bias mass" corrections to experimental data (see Reference A1) due to hidden contour effects are roughly equivalent to the total mass removed. Increasing the dust field concentration increases the possibility of "predamage", but it also increases other factors, such as heating augmentation (see Section 4) and relative certainty in the data. Thus there is a tradeoff in the ability to discriminate phenomena as the field density increases.

Aside from these qualifications, calculations of surface temperatures on a model in the BR using existing analytical models give temperatures at representative flight cloud densities which are well above those of the data base for SI (see Section 4.2), as do the measured BR surface temperatures of Jones (Reference A1). The results of Section 3.2.3 suggest that SI mass loss may significantly increase with temperature as it approaches the point where the values of mechanical strength properties approach zero (perhaps 7500°R). Thus, it becomes important in terms of rationalizing the two kinds of data to increase the temperature range for the SI data base and/or to decrease the heating rate in the BR so as to bring the two into near equality. If the preceding considerations about velocity and dust field concentration are taken as fixing the value of these variables, then the obvious choice is to lower the BR range pressure. This can be done to a certain extent, limited however, by the requirements for flight stability of the model. Nevertheless, it is possible to find a set of BR conditions (velocity, range pressure and field concentration) that match the surface state of the target to that attainable in SI experiments. This has been done using current computer codes and a matrix of calculations specifically structured to search out the desired values. The results of these calculations are reflected in the test matrix of Section A.5.

A.3 MATERIAL SELECTION AND SAMPLE PREPARATION

Among the many possible sources of uncertainties, some of those that may still affect the data of both SI and BR experiments, given the degree of similitude outlined in the previous section, can be argued to be related to statistical variation of material strength and failure characteristics. Support for this conjecture is presented in Section 3.3, which gives a first order estimate of the variance of single impact mass loss resulting from random selection of material samples as $\pm$30 percent to $\pm$40 percent of the mean. This estimate is based on available statistics (covering a time span of several years) of material strength properties of ATJ-S graphite. It is probably an over estimate of what is achievable when samples are carefully selected from billets currently available. However, in spite of the fact that ATJ-S is probably one of the most well known (in terms of its properties) nosetip materials it is still likely that irregularities in grain size and other inhomogeneities and differences in anisotropies contribute to scatter in both SI and BR experiments. Indications of these granularity effects can be inferred from the scanning electron microscope photographs of SI craters given by Rubin and McClelland (Reference A7).

In order to reduce uncertainties of this kind as much as possible, it is recommended that cylindrical sections (~0.75 in diameter) be machined from pieces taken from recorded

location in a billet. The sections should be cut, identified and machined into samples that are oriented so that the model surface subjected to SI and BR testing (at the matched conditions) are closely related to the surfaces of the original cut.

The preferred material is ATJ-S graphite because of its relative uniformity (compared to composites) of structure and manufacturing method. The smallest number of reasonably small sized billets (consistent with the total number of required test samples) should be used to further decrease sample variability.

In addition to the outline of the concepts behind the proposed test plan given in the foregoing, there are some specific details on current experimental procedures and arrangements of apparatus that are of questionable efficacy. These questions are discussed in the next section, and some suggestions for improved experimental methods are offered. The test matrix is given in Section 5 which is followed by an explanation of the proposed method of data analysis.

A.4 EXPERIMENTAL PROCEDURES

The basic premise of closely controlled samples being tested in parallel in the ballistic range and in single impact facilities has been discussed in previous sections of this appendix. In this section, some of the special problems of these two types of erosion testing techniques are considered separately and some changes in methodology are suggested.

It should be noted first, that it is recognized that both SI and BR tests present significant challenges to the skills and the ingenuity of an experimentalist. The progress that has been made is testimony to the highly competent way in which rather difficult experiments have been undertaken. However, it is believed that further improvement in the experiments is needed and can be realized. To this end, the following suggestions and possible lines of development are proposed.

A.4.1 Single Impact Experiments

Generally, it appears that current practice in SI tests produces results that are of good quality (see Section 3.1 for a summary of estimated errors in SI experiments). The desired improvements of SI tests is not so much a matter of technique as it is the need to extend the upper limits of the temperature range over which the experiments are carried out.

The existing methods of achieving high surface temperature by induction or plasma jet heating presently give data up to about 5500°F, but could probably be extended to reach 6500°F

(Graham (Reference A4)). For both methods, changes in target mass from effects other than particle impact are increased and lead to further uncertainties in the data. This seems to be a necessary consequence of conducting SI tests at temperatures approaching the sublimation temperature of carbon (approximately 7200°R at 1 atm). The current practice of inferring mass loss from crater volume measurements (rather than weighing the sample) is a result of these problems.

Of the two heating methods presently available, it is judged that there is less overall uncertainty associated with induction heating than with the plasma jet, but that it would be better if a cleaner and more predictable method were devised. It has been suggested by Laub (Reference A8) that laser heating is feasible and this appears to be an idea that is worth pursuing. The apparent advantages are that the heating times could be made comparable to those found in a ballistic range, and that the time delay between the heating and the impact could be reduced to essentially zero. This would result in SI sample in-depth temperature distributions closer to those found in the BR, which may be important as discussed in Subsection A.2.2.

According to Graham (Reference A4), current SI induction heating cycles are of the order of 5 to 10 seconds, resulting in nearly uniform in-depth temperature distributions for carbon. By comparison, heating of the model in the AEDC Range G occurs in a few milliseconds.

An existing laser facility at NASA Ames (Lundell, et al. (Reference A9)) has an output power level of 40 kw distributed over a 1 inch diameter beam. This facility, for example, would give a heating rate of 7000 Btu-sec^{-1}ft^{-2} compared to 2000 Btu-sec^{-1}ft^{-2} for the plasma jet and to the 25 kw of the induction heater (which is not directly coupled to the specimen) that are currently in use at Effects Technology, Incorporated (Graham (Reference A4)). Thus, SI sample heating times could be significantly decreased using a system similar to the Ames laser. Another possible advantage is that laser heating may be controlled enough so that accurate ablation predictions of the mass lost by the sample during the heating cycle can be obtained.

Therefore, it appears that an experimental technique based on this idea is practical and potentially a significant improvement over current methods.

A.4.2 Ballistic Range Experiments

The comments given here on the environment in a ballistic range are based on a comparison with reentry conditions, in contrast to th main theme of this appendix of compatibility with single impact tests. The reason for this digression is that there appears to be an aspect of the BR dust field that is unlike a natural cloud and may lead to sources of error when extension to flight is considered.

In a cloud with a mass concentration, w, particles of diameter, d_p, and mass density, ρ_p, the average number density, N, is given by

$$N = \frac{6w}{\pi \rho_p d_p^3}$$

In a natural cloud, particle diameters are distributed over some range (usually exponentially) and this simple expression then involves an integral over the distribution function which is slightly more complicated but not different in kind. However, the above expression is appropriate for a dust environment of uniform partic size. It is consequently expected that a reasonable estimate of the mean distance between particles in a cloud is*

$$\ell_m = N^{-1/3} = \left(\frac{\pi \rho_p}{6w}\right)^{1/3} d_p$$

For the dust field in its present configuration, and with a typical hemispherical model, then

$$\bar{V} = \pi R_N^2 L = 0.6J \text{ ft}^3$$

where $\bar{V}$ = volume swept out by a BR model

L = 440 ft = range length

R_N = 0.25 in. = nose radius

---

*In natural weather, a cloud is in a state of turbulent motion and it is known that this results in local accumulations of high concentrations of suspended particulate matter due to the uneven convection of different particle sizes by turbulent eddys of different scales and intensities. Hence, the variance of local distances between particles in a cloud may be quite large fractions of the mean and it may require averaging over a volume much larger than $(\ell_m)^3$ to obtain a stable estimates.

It is possible to estimate the average free flight distance between impacts on a model. This is done in Table A1 for a series of dust field concentrations ranging from 0.056 to 3.20 gm/m^3. It is seen that one impact at every plate (in the present configuration of 40 plates at approximately 11 ft intervals – intervals actually vary between about 7 and 14 feet) is expected if w = 0.10 gm/m^3, or one impact every other plate at w = 0.056 gm/m^3. However, at higher concentrations, say w ~ 1.0 gm/m^3, the present configuration would given approximately 10 hits at each of the 40 dust generators. This is more like a series of step functions interspersed with flight through a clear environment, which does not appear to simulate flight.

Even at 10 hits per generator it is probable that at a given uniform surface temperature the impacts can be considered as separate but parallel events in terms of the magnitudes, eroded mass and surface roughness. Perhaps the most significant direct effect of lack of simulation is in terms of erosion augmented heat and mass transfer. These effects are almost certainly felt even in regions reasonably removed from the actual impact sights, and dependent upon disturbance frequency. It is postulated that small disturbances at high frequency ($f \propto wu_\infty/\rho_p d_p$ in flight) have a more profound effect on convective augmentation than the large disturbances at relatively low frequency ($f \propto u_\infty$, independent of ρ_p, d_p, and w for values of w greater than about 0.1 gm/m^3) associated with the present erosion field arrangement.

Indirect effects due to this type of lack of field simulation relate to influences of surface temperature on erosion. If convection augmentation phenomena are not simulated mean surface temperatures will be in error. Secondly, considerations of discrete versus continuous effects on surface temperature suggest that a more uniform field is desirable (consider, for example, multidimensional boundary layer and subsurface heat flows, during the intervals of time between impacts).

Therefore, it would be useful if the dust field could be spread out more evenly over the 440-foot range length. Table A1 shows that the range of interest for the mean distance between particles is from 3 cm to 10 cm. A redesign of the dust field generators that would produce a more realistic spatial distribution is desirable and should be considered. There appear to be even fewer difficulties in implementing these objectives in the case where environment is rain instead of dust.

It is recognized that a particulate field in the ballistic range with characteristics of this kind requires some changes in methodology for the measurement of impacted mass. The current practice of using 20 cameras (focused on alternate dust fields) to photograph the

TABLE A1. ESTIMATED CONTINUUM FIELD SIMULATION REQUIREMENTS IN BALLISTIC RANGE

w (gm/m²)	N (no/m³)	ℓ_m (cm)	n_i	L (ft)	$\frac{f_1}{u_\infty}$ (ft^{-1})	$\frac{f_2}{u_\infty}$ (ft^{-1})
0.056	1,207	9.4	21	21.0	0.048	0.048
0.10	2,155	7.7	37	11.9	0.084	0.084
0.18	3,879	6.4	66	6.7	0.150	0.091
0.32	6,897	5.3	117	3.8	0.26	0.091
0.56	12,069	4.4	205	2.1	0.47	0.091
1.00	21,552	3.6	366	1.2	0.83	0.091
1.80	38,793	2.9	659	0.7	1.50	0.091
3.20	68,996	2.4	1172	0.4	2.66	0.091

n_i = total number of hits on 0.25 in. dia. model in 440 ft.

w = mean free flight distance between impacts

f_1 and f_2 are expected frequencies of impact on the model nose for uniform and the present fields, respectively

300 μm diameter dust particle

area that the model intercepts, will (if the particles are more uniformly dispersed) give data that need to be interpreted differently. Such data, in this case, would amount to samples of a nearly continuous particulate field.

In summary, it seems appropriate to specify an erosive field in terms of the average properties used in a flight prediction, and, if the BR lacks certain aspects of the needed simulation (because of short field length, for example) these deficiencies should not be exaggerated by further deviations from accurate simulation. In addition, it is suggested that shots through well defined dust fields be repeated until the accumulated average total recession becomes stable. Thus, the inevitably statistical nature of BR results due to the short range length and statistical properties of the erosion field could be reasonably averaged without undue interference with the similitude.

A.5 TEST MATRIX

The test plan given in this section has some features in common with current (Herbig, Reference A10) and proposed (Benjamin, et al. (Reference A6)) programs in the AEDC BR. This reflects the fact that, to a certain extent, others recognize similar needs for the test results. However, the need to combine SI and BR tests has recently come into focus and created the opportunity to use this combination as leverage for improving the overall results. This is the major departure taken by the test matrix shown in Table A2.

As indicated in the table, the first series of experiments, 12 each SI and BR tests, follows the ideas explained earlier for matching the environmental conditions as closely as possible and for maintaining a high degree of correlation of material properties between the samples. The BR range pressure and field concentration combination shown in the XY-1 series was calculated employing continuum steady state modeling to give the surface temperature currently possible in SI tests (~6000°F), assuming a single impact mass loss ratio fit to recent data (Reference A7). Thus the test matrix assumes the use of current facilities. If higher temperatures become available for SI tests, the conditions could be adjusted. It should also be noted that Table A2 shows a higher than usual number of repeats at a given set of nominal conditions. This follows from the arguments given previously about the uncertainties in BR data, but also is thought to be cost effective if tare shots are dispensed with (as is the case here).

The minimum field density in Table A2 is chosen as a compromise to satisfy several ballistic range testing and test objective constraints described below:

TABLE A2. TEST MATRIX – COMBINED SINGLE IMPACT/BALLISTIC RANGE EXPERIMENTS

Ballistic Range				Single Impact		
Sample-Series	Velocity (kfps)	Pressure (mmHg)	Concentration (gm/m^3)	Sample-Series	Velocity (kfps)	Temperature (°R)
AB-1	18	50	0.28	CB-1	18	6250
CD-1	18	50	0.28	ED-1	18	6250
EF-1	18	50	0.28	GF-1	18	6250
GH-1	18	50	0.28	IH-1	18	6250
AB-2	18	*100	0.43	CB-2	18	6250
CD-2	18	100	0.43	ED-2	18	6250
EF-2	18	100	0.43	GF-2	18	6250
GH-2	8	100	0.43	IH-2	18	6250
AB-3	18	*230	0.77	CB-3	18	6250
CD-3	18	230	0.77	ED-3	18	6250
EF-3	18	230	0.77	GF-3	18	6250
GH-3	18	230	0.77	IH-3	18	6250

All samples from one billet of ATJ-S; Sample-Series designates adjacent cuts (second letter is test surface) – billet section; all tests with 300 μm glass beads.

*Range pressure and concentration calculated to give surface temperature of 6250°R with erosion augmented heating.

- Minimum range pressure of 50 mm Hg to provide model stability
- Minimum cloud concentration to obtain 1-2 surface obscurations during traversal of the field, to minimize multiple impact effects while obtaining sufficiently measurable recession (0.030" - 0.050")
- Maximum concentration at the minimum pressure to obtain a surface temperature greater than 6000°R based on continuum erosion considerations (note that higher Si surface temperatures will enable lower field densities at lower obscuration and smaller but measurable recessions)

Tests with higher than minimum field densities are also presented in Table A2, with range pressures adjusted to maintain the desired surface temperature (Series XY-2, XY-3). The necessary magnitudes of pressure depend upon pressure effects on erosion augmented heat and mass transfer.* The tests are planned to maintain a parallel SI matrix as in the XY-1 series. They will also show increasing effects of multiple impacts relative to material preconditioning, and impact frequency relative to augmented convection.

The conditions for these tests are such that thermochemical ablation will be about 10 percent of the total recession, approximately independent of the field density for the range of densities considered. Higher ratios of thermochemical to total recession at fixed surface temperature are obtained as model velocities are lowered, with expectations of about 15 percent and 25 percent for velocities of 15 kfps and 12 kfps, respectively. Accordingly, additional tests are recommended at these lower velocities as presented in Table A3, where as before, pressures have been selected to maintain constant model surface temperature while employing the same values of cloud densities as used for 18 kfps tests. The numbers of repeat shots in these series are smaller than the 18 kfps series, in anticipation that positive benefits in terms of data repeatability will be derived from careful control of material conditions. Appropriate SI tests should also be conducted in concert with these later tests.

The recommended program in summary has the following significant features, some of which have not been discussed previously:

- A single dust particle size, in order to control shock layer traversal effects, and selected to be compatible with both SI and BR tests

*For fixed velocity and surface and free stream temperatures, it can be shown that required cloud concentrations vary approximately with $p_\infty^{0.63}$ based on existing erosion augmentation correlations.

TABLE A3. TEST MATRIX — BALLISTIC RANGE

Sample-Series	Velocity (kfps)	Pressure (mmHg)	Concentration (gm/m^3)
AB-4	15	80*	0.28
CB-4	15	80*	0.28
CD-4	15	150*	0.43
ED-4	15	150*	0.45
AB-5	15	340*	0.77
CD-5	15	340*	0.77
EF-5	12	130*	0.28
GH-5	12	130*	0.28
AB-6	12	240*	0.43
CD-6	12	240*	0.43
EF-6	12	570*	0.77
GH-6	12	570*	0.77

- Conditions chosen to obtain all results at approximately constant surface temperature, enabling a correlation of BR and SI experiments, and possible correlation of convective augmentation effects, multiple impact effects, etc., without introduction of extraneous effects which are attributable to wall temperature variations
- Surface temperature selected to be within capabilities of both SI and BR capabilities; to be low enough to eliminate concerns about sublimation kinetics for the range of pressures that will exist; to be high enough to eliminate possible concerns of oxidation kinetics; and to be high enough to represent the lower range of temperatures to be expected in a real flight environment
- Field densities selected to be high enough to provide low percentage uncertainties in the ablated/eroded mass, and as low as possible in terms of obscuration to minimize multiple impact effects while maintaining model stability and surface temperature
- Range of cloud densities selected to be representative of the upper range in natural environments
- Careful attention devoted to minimizing the causes for data scatter while maximizing the conditions for good correlation between SI and BR tests.

The discussions thus far are not intended to suggest that the above test program is really comprehensive. Additional parameters of major concern include considerations of particle size and density (as they are expected to influence convective augmentation in contrast to erosion behavior; obscuration; and continuum versus discrete behavior), and variants with surface temperature and material. The above program is believed to be sufficiently comprehensive in terms of demonstrating a systematic approach to coupled erosion evaluations, experimental and analytical.

A.6 ANALYSIS OF COUPLED EROSION/ABLATION DATA

Conditions upstream of the erosion field should be selected so as to yield preimpact surface temperatures which are somewhat greater than those expected during erosion. The purpose here is to minimize the extent of transient effects of the model behavior as it traverses the erosion field.

The data analysis should include the following:

1. Construction of a nomograph or series of charts to determine the sensitivity of surface temperature and surface recession rate to erosion rate, heat transfer coefficient, mass transfer coefficient, and model velocity. For simplicity, steady state continuum techniques should be employed for this analysis.

2. Pre- and post-test transient state continuum analyses should be performed. Input and modeling for pretest analyses should be based on the latest formulations in existence at the time. Post-test analysis should use combinations of mathematical modeling and time variant input parameters, chosen in such a way as to provide best agreement between predicted and experimentally observed surface temperatures and recession rates. Guidance for the optimum choice of the values of parameters should be based on the data generated in Item 1 above.

3. Analyses should include the time span of the complete trajectory, with appropriate modeling to account for crater healing and other transient effects as the model leaves the cloud.

4. Selective analyses of discrete effects, and multidimensional flow effects should be performed to account for the known physics not included in the analysis in Item 2 above.

5. Analyses and experiments should be scheduled so as to provide optimum yield from both.

Through the above analysis procedures, it is believed that maximum value can be derived from the recommended test program. In particular, it is believed that the data analysis can provide information on erosion and associated phenomena that is substantially free of uncertainties and quite applicable to flight situations. This applicability is both direct by virtue of the realism of test conditions, and indirect by virtue of the basic data which will be provided for mathematical modeling purposes.

REFERENCES FOR THE APPENDIX

A1. Jones, G. R., "SAMSO/Aerospace Snow/Dust Erosion Tests (U)," Preliminary Data Package, Project V41G-34A, AEDC-ARO Incorporated, February 1975 (SECRET).

A2. Kreyenhagen, K. N., Wagner, M. H., and Goerke, W. S., "Direct Impact Effects in Hypersonic Erosion," SAMSO-TR-73-339, August 1973.

A3. Jaffe, N. A., "Hydrometeor Shock Interactions," Aerotherm/Acurex Interim Report, Contract DNA001-74-C-0051, March 15, 1975, (Final Report in preparation).

A4. Graham, M., personal communication, Effects Technology, Incorporated, Santa Barbara, California.

A5. Benjamin, A. S., "Hypersonic Erosion Facilities Comparison and Rain, Dust and Ice Correlations (U)," AFML-TR-73-233.

A6. Benjamin, A. S. and Sergeant, R. J., "Erosion Data Analysis Program (U)," First Semi-Annual Report, TRW-25763-6001-RE-00, March 1975.

A7. Rubin, L. and McClelland, J., "The Influence of Temperature on Hypervelocity Erosion of Graphite," Aerospace Corporation, El Segundo, California. Paper presented in Fourth International Conference on Rain Erosion and Associated Phenomena in Meiroburg, Federal German Republic, May 1974.

A8. Laub, B., personal communication, Aerotherm Division/Acurex Corporation, Mountain View, California.

A9. Lundell, J. H., Offen, L. J., and Dickey, R. R., "The CO_2 Gasdynamic Laser as a High-Intensity Radiation Facility," AIAA Paper No. 75-177, January 1975.

A10. Herbig, W., private communication, Aerospace Corporation, El Segundo, California.